Multiscale computational homogenization methods with a gradient enhanced scheme based on the discontinuous Galerkin formulation

V.-D. Nguyen[a], G. Becker[a], L. Noels[a,*]

[a] *University of Liege (ULg),*
Department of Aerospace and Mechanical Engineering Department,
Computational & Multiscale Mechanics of Materials
Chemin des Chevreuils 1, B-4000 Liège, Belgium

Abstract

When considering problems of dimensions close to the characteristic length of the material, the size effects can not be neglected and the classical (so–called first–order) multiscale computational homogenization scheme (FMCH) looses accuracy, motivating the use of a second–order multiscale computational homogenization (SMCH) scheme. This second–order scheme uses the classical continuum at the micro–scale while considering second–order continuum at the macro–scale. Although the theoretical background of the second–order continuum is increasing, the implementation into a finite element code is not straightforward because of the lack of high–order continuity of the shape functions. In this work, we propose a SMCH scheme relying on the discontinuous Galerkin (DG) method at the macro–scale, which simplifies the implementation of the method. Indeed, the DG method is a generalization of weak formulations allowing for inter-element discontinuities either at the C^0 level or at the C^1 level, and it can thus be used to constrain weakly the C^1 continuity at the macro–scale. The C^0 continuity can be either weakly constrained by using the DG method or strongly constrained by using usual C^0 displacement–based finite elements. Therefore, two formulations can be used at the macro–scale: (i) the full–discontinuous Galerkin formulation (FDG) with weak C^0 and C^1 continuity enforcements, and (ii) the enriched discontinuous Galerkin formulation (EDG) with high–order term enrichment into the conventional C^0 finite element framework. The micro–problem is formulated in terms of standard equilibrium and periodic boundary conditions. A parallel implementation in three dimensions for non–linear finite deformation problems is developed, showing that the proposed method can be integrated into conventional finite element codes in a straightforward and efficient way.

Keywords: Second–order, Discontinuous Galerkin, Periodic condition, FEM, Computational homogenization, Heterogeneous materials

1. Introduction

Nowadays, the numerical simulation of engineering applications with heterogeneous materials poses many mathematical and computational challenges. In theory, such problems can be directly solved by using a standard finite element procedure. However, it requires the mesh size h to be smaller than the heterogeneities size, i.e. $\epsilon : h < \epsilon$, and if ϵ is small, the simulation may not be performed due to the enormous number of the degrees of freedom. An effective remedy, which is known as the computational homogenization, has been developed to link up straightforwardly the responses of the large scale problems, also called the macroscopic problems, to the behavior of the smaller scale problems, also called the microscopic problems, where the presence of heterogeneities is considered. The basic ideas of the computational homogenization approach have been presented in papers by Michel et al. [1], Terada et al. [2], Miehe et al. [3, 4], Kouznetsova et al. [5, 6, 7], Kaczmarczyk et al. [8], Peric et al. [9], Geers et al. [10] and references therein, as a non–exhaustive list. By this technique, two boundary value problems are defined at two separate scales,

*Corresponding author; Phone: +32 4 366 4826; Fax: +32 4 366 9505
Email address: L.Noels@ulg.ac.be (L. Noels)

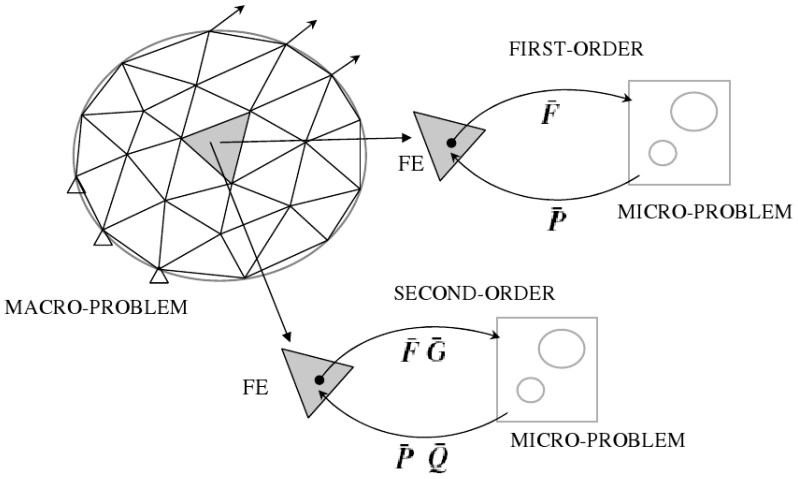

Figure 1: Illustration of first–order and second–order multiscale computational homogenization schemes. The deformation gradient $\bar{\boldsymbol{F}}$ and the first–order stress $\bar{\boldsymbol{P}}$ are used in the first–order scheme while the gradient of deformation gradient $\bar{\boldsymbol{G}} = \bar{\boldsymbol{F}} \otimes \boldsymbol{\nabla}_0$ and the higher–order stress $\bar{\boldsymbol{Q}}$ are added to capture the high–order effects in the second–order scheme.

one is defined at the microscopic scale and one is defined at the macroscopic scale. Such an approach does not require the macroscopic constitutive response to be known a priori and enables the incorporation of both geometrical and material non–linearities [11]. The macroscopic material law is extracted from the analysis of the microscopic boundary value problem (BVP), which is defined by a representative volume element (RVE) with a suitable boundary condition related to the macroscopic quantities. This procedure does not lead to a closed–form of the macroscopic constitutive law, but the stress–strain relation is always available through the resolution of the BVPs.

The classical multiscale computational homogenization approach (so–called the first order multiscale computational homogenization approach – FMCH) provides a versatile tool to model the micro–macro transitions and is based on the standard continuum theory [1, 2, 3, 4, 5, 9, 10]. For a given macroscopic deformation gradient tensor, the stress and the associated material tangent are estimated from the response of the micro–structure, see Fig. 1. Similar first order computational homogenization schemes have also been developed for material layers [12]. Although the first–order scheme accounts for the volume fraction and for the microscopic morphology, the influence of the absolute size of the constituents at the micro–scale is not considered. Indeed, the separation of scales must be satisfied in order to capture the equivalent homogeneous state by analyzing the microscopic problem according to the local action principle. However, this condition is sometimes violated when the macroscopic length scale and the microscopic length scale gets closer. In this case, the classical FMCH procedure would lead to a solution which is not physical because of the violation of the local action principle. Therefore the classical homogenization procedure cannot capture the high gradient at the RVE level and the size effects cannot be captured in the regions of high deformation gradients [6].

To be able to cover the localization and size effect problems at a given resolution scale, many authors have proposed to use generalized continuum formulations (e.g. Cosserat, couple–stress, strain–gradient, non–local, micromorphic formulations), see [13, 14, 15, 16, 17, 18, 19] amongst others. In the generalized continuum theory, the length scale is introduced into the material constitutive law and the method is able to capture the size effects. For the multiscale problems, the generalized continuum can potentially be used at both the macroscopic and the microscopic scales. Recent extensions of the FMCH scheme to the second–order continuum, as for the so–called second–order multiscale computational homogenization (SMCH) [6, 7, 8], provide a systematic way to couple the strain–gradient continuum at the macro–scale with the classical continuum at the micro–scale, see Fig. 1. In this scheme, both the deformation gradient and its gradient are used at each macroscopic material point to define the microscopic boundary condition. The macroscopic stress and higher–order stress are computed by using the generalized version of the Hill–Mandel macro–homogeneity condition.

To solve the strain–gradient problem at the macro–scale, the addition of the high–order terms in the generalized internal virtual work leads to many complications in the numerical treatment of the finite element framework. With

the conventional displacement–based finite element method, this requires not only the continuity of the displacement field but also the continuity of its first derivatives. In other words, at least the C^1 continuity of the interpolation shape functions must be used. When solving the strain–gradient problems, the C^1 finite elements have been successfully developed, see [20, 21]. Alternative approaches consider a mixed formulation [22, 23], or the micromorphic formulation [19] from which the strain gradient formulation can be recovered. The strategy of introducing another unknown field beside the unknown displacement field in the C^1 element, the mixed formulation and in the micromorphic formulation raises the number of degrees of freedom. Therefore, the use of the C^0 conventional continuous elements is favored. Another effective approach is the continuous– discontinuous Galerkin (C^0/DG) method [24, 25]. This approach, which uses C^0 continuous interpolation functions, is formulated in terms of the displacement unknowns only and weakly enforces the continuity of the higher–order derivatives at the inter–element boundaries by using the DG formulation. However, in the mentioned works, only linear elastic materials are considered. In this paper a one–field DG formulation of the strain–gradient theory for finite strains is required.

As a generalization of weak formulations, DG methods allow for the discontinuities of the problem unknowns in the interior of the domain, see [26, 27] and their references. The domain is divided into sub–domains on which the integration by parts is applied, leading to boundary integral terms on the subdomain interfaces involving the discontinuities. The role of these terms is to enforce weakly the consistency and the continuity of the problem unknowns. When considering problems involving high–order derivatives, the DG method can also be seen as a way of imposing weakly the high–order continuity. This advantage has been exploited in the mechanics of beams and plates [24, 28], of shells [29], and of Mindlin's theory [24, 25]. When using DG methods, the jump discontinuities can be related to the unknown fields and their derivatives or to their derivatives only. The DG methods have also been developed for strain–gradient damage [30] and for gradient plasticity [31, 32], where the discontinuity of the equivalent strain across inter–element interfaces is weakly enforced. In mathematical analyzes, the DG methods were also used to impose weakly the C^0 continuity of the displacement field [33, 34] when solving, at the macro–scale, multiscale elliptic problems.

The purpose of this work is to establish a second–order multiscale computational homogenization for finite deformations based on the DG formulation at the macro–scale, while the micro–problem is formulated in terms of standard equilibrium and boundary conditions. The DG method is used to constrain weakly the C^1 continuity by inter–element integrals. The C^0 continuity can be either weakly imposed by the DG formulation or strongly constrained using the conventional C^0 displacement–based finite element. Thus two formulations can be used:

- the full DG formulation (FDG), which constrains weakly the C^0 and C^1 continuities, and
- the enriched DG formulation (EDG) with high–order term enrichments into the conventional C^0 finite element framework.

Considering a DG formulation allows traditional finite element to be considered although the strain–gradient continuum is used. Furthermore, as the shape functions remain continuous with the EDG formulation, the number of degrees of freedom in this case is the same as for conventional C^0 finite elements. On the contrary, the FDG method suffers from an explosion in the number of degrees of freedom as the the shape functions are now discontinuous. Nevertheless the FDG formulation is advantageous in case of parallel implementations using face–based ghost elements [35, 36]. 3–dimensional implementations of both the EDG and FDG methods are presented in this paper, showing that they can be integrated into conventional parallel finite element codes without significant effort. Non–linear multiscale applications are then presented to demonstrate the efficiency of the method.

The organization of the paper is as follows. In section 2, the problem statement of the SMCH is recalled. The solution of the macroscopic boundary value problem by a one–field DG formulation is developed in the section 3. The section 4 presents the resolution of the microscopic problem with periodic boundary conditions arising from the multi–scale framework. To demonstrate the SMCH efficiency, an example with size effects is provided in section 5.

2. Multi–scale problem formulation

The second–order multiscale computational homogenization, which is extended from the classical one, is a full gradient geometrically non–linear approach pioneered in [6]. This procedure uses the macroscopic deformation gradient tensor and its gradient to prescribe the essential boundary condition on the microscopic boundary value problem.

In this framework, all microscopic boundary value problems are treated as a classical continuum using the standard state equations and constitutive laws. A brief review of the formulation of the second–order continua macro–problem and of the associated microscopic problem is now presented.

2.1. Problem at the macroscopic scale

In this section, the Mindlin strain gradient problem [16] is briefly recalled. The body B, whose reference configuration is B_0, undergoes the deformation characterized by the mapping $\bar{\boldsymbol{\varphi}} : B_0 \rightarrow B \,|\, \bar{\boldsymbol{x}} = \bar{\boldsymbol{\varphi}}(\bar{\boldsymbol{X}})$, where $\bar{\boldsymbol{x}} \in B$ and $\bar{\boldsymbol{X}} \in B_0$ are respectively the current and reference positions of the material point. The displacement field is defined by

$$\bar{\boldsymbol{u}} = \bar{\boldsymbol{x}} - \bar{\boldsymbol{X}} = \bar{\boldsymbol{\varphi}}(\bar{\boldsymbol{X}}) - \bar{\boldsymbol{X}} \,. \tag{1}$$

The internal virtual work is assumed to be determined by the deformation gradient tensor $\bar{\boldsymbol{F}} = \bar{\boldsymbol{x}} \otimes \boldsymbol{\nabla}_0 = \boldsymbol{I} + \bar{\boldsymbol{u}} \otimes \boldsymbol{\nabla}_0$ and by its gradient $\bar{\boldsymbol{G}} = \bar{\boldsymbol{F}} \otimes \boldsymbol{\nabla}_0 = \bar{\boldsymbol{u}} \otimes \boldsymbol{\nabla}_0 \otimes \boldsymbol{\nabla}_0$ combined with their conjugated stresses, which are respectively the first Piola-Kirchhoff stress tensor $\bar{\boldsymbol{P}}$ and the higher–order stress tensor $\bar{\boldsymbol{Q}}$. The higher–order gradient and higher–order stress have the symmetrical properties $\bar{G}_{ijk} = \bar{G}_{ikj}$ and $\bar{Q}_{ijk} = \bar{Q}_{ikj}$. The internal virtual work [14, 15, 17] is generalized to the finite strain case by the relation [11]

$$\delta W_{\text{int}} = \int_{B_0} \left(\bar{\boldsymbol{P}} : \delta\bar{\boldsymbol{F}} + \bar{\boldsymbol{Q}} \vdots \delta\bar{\boldsymbol{G}} \right) dB \,, \tag{2}$$

where the double dot product is defined by $\bar{\boldsymbol{P}} : \delta\bar{\boldsymbol{F}} = \bar{P}_{ij}\delta\bar{F}_{ij}$ and where the triple dot product is defined by $\bar{\boldsymbol{Q}} \vdots \delta\bar{\boldsymbol{G}} = \bar{Q}_{ijk}\delta\bar{G}_{ijk}$.

The body B_0 is subjected to a body force $\bar{\boldsymbol{B}}$ and to boundary conditions. For the Mindlin strain gradient theory [16], the prescribed boundary conditions are low–order and higher–order conditions, which must be independently defined at any point at the surface of the body ∂B_0. The low–order boundary conditions are applied as in the classical continuum theory by dividing the boundary ∂B_0 into the Neumann part $\partial_N B_0$ subjected to a prescribed traction $\bar{\boldsymbol{T}}^0$ and into the Dirichlet part $\partial_D B_0 = \partial B_0 \backslash \partial_N B_0$ subjected to the prescribed displacement $\bar{\boldsymbol{u}}^0$, such that

$$\bar{\boldsymbol{u}} = \bar{\boldsymbol{u}}^0 \quad \forall \bar{\boldsymbol{X}} \in \partial_D B_0 \text{ and} \tag{3}$$

$$\bar{\boldsymbol{T}} = \bar{\boldsymbol{T}}^0 \quad \forall \bar{\boldsymbol{X}} \in \partial_N B_0 \,, \tag{4}$$

where the surface traction $\bar{\boldsymbol{T}}$ by unit of reference surface will be defined later. The higher–order boundary conditions either constrain the normal gradient of the displacement field $D\bar{\boldsymbol{u}}$, with the normal gradient operator $D(.) = \bar{\boldsymbol{N}} \cdot \boldsymbol{\nabla}_0(.)$ obtained from the outward unit normal $\bar{\boldsymbol{N}}$ of the reference body, or the double stress traction $\bar{\boldsymbol{R}}$. The displacement gradient component normal to the surface $(\bar{\boldsymbol{N}} \cdot \boldsymbol{\nabla}_0)\bar{\boldsymbol{u}}$ is considered to apply the boundary conditions instead of the complete displacement gradient $\bar{\boldsymbol{u}} \otimes \boldsymbol{\nabla}_0$ since the latter is not independent from the value of $\bar{\boldsymbol{u}}$ on the surface. The kinematically admissible sets of boundary conditions are thus chosen in terms of $\bar{\boldsymbol{u}}$ and $D\bar{\boldsymbol{u}}$ in order to have a unique solution. The higher–order boundary conditions are thus applied by dividing the boundary ∂B_0 into the $\partial_M B_0$ part, which undergoes the double stress traction $\bar{\boldsymbol{R}}^0$, and into the $\partial_T B_0 = \partial B_0 \backslash \partial_M B_0$ part, where the normal gradient of displacement is constrained to $D\bar{\boldsymbol{u}}^0$, such that

$$D\bar{\boldsymbol{u}} = D\bar{\boldsymbol{u}}^0 \quad \forall \bar{\boldsymbol{X}} \in \partial_T B_0 \text{ and} \tag{5}$$

$$\bar{\boldsymbol{R}} = \bar{\boldsymbol{R}}^0 \quad \forall \bar{\boldsymbol{X}} \in \partial_M B_0 \,, \tag{6}$$

where the double stress traction is defined by $\bar{\boldsymbol{R}} = \bar{\boldsymbol{Q}} : (\bar{\boldsymbol{N}} \otimes \bar{\boldsymbol{N}})$.

In continuum mechanics, the weak form of the problem is stated as finding the continuous displacement field $\bar{\boldsymbol{u}} \in \mathbf{H}^p$, where $\mathbf{H}^p$ is the Hilbert space of degree p in $\mathbb{R}^3$, for which the internal virtual work is equal to the external one. By using Eq. (2), the problem statement is to find $\bar{\boldsymbol{u}} \in \mathbf{H}^4(B_0)$ such that

$$\int_{B_0} \left(\bar{\boldsymbol{P}} : \delta\bar{\boldsymbol{F}} + \bar{\boldsymbol{Q}} \vdots \delta\bar{\boldsymbol{G}} \right) dB = \int_{B_0} \bar{\boldsymbol{B}} \cdot \delta\bar{\boldsymbol{u}} \, dB + \int_{\partial_N B_0} \bar{\boldsymbol{T}} \cdot \delta\bar{\boldsymbol{u}} \, d\partial B + \int_{\partial_M B_0} \bar{\boldsymbol{R}} \cdot D\delta\bar{\boldsymbol{u}} \, d\partial B \quad \forall \delta\bar{\boldsymbol{u}} \in \mathrm{U}_c \left(B_0 \right), \tag{7}$$

where $\mathrm{U}_c(B_0) = \{\delta\bar{\boldsymbol{u}} \in \mathbf{H}^4(B_0) \,|\, \delta\bar{\boldsymbol{u}} = \mathbf{0}\, \forall \bar{\boldsymbol{X}} \in \partial_D B_0$ and $D\delta\bar{\boldsymbol{u}} = \mathbf{0}\, \forall \bar{\boldsymbol{X}} \in \partial_T B_0\}$. By using the Gauss theorem, the first term of the internal energy yields

$$\int_{B_0} \bar{\boldsymbol{P}} : \delta\bar{\boldsymbol{F}}\, dB = \int_{\partial B_0} \delta\bar{\boldsymbol{u}} \cdot \left(\bar{\boldsymbol{P}} \cdot \bar{\boldsymbol{N}}\right) d\partial B - \int_{B_0} \delta\bar{\boldsymbol{u}} \cdot \left(\bar{\boldsymbol{P}} \cdot \boldsymbol{\nabla}_0\right) dB \quad \forall \delta\bar{\boldsymbol{u}} \in \mathrm{U}_c(B_0)\,, \tag{8}$$

while the second term leads to

$$\begin{aligned} \int_{B_0} \bar{\boldsymbol{Q}} \vdots \delta\bar{\boldsymbol{G}}\, dB \quad &= \int_{\partial B_0} \left(\bar{\boldsymbol{Q}} \cdot \bar{\boldsymbol{N}}\right) : (\delta\bar{\boldsymbol{u}} \otimes \boldsymbol{\nabla}_0)\, d\partial B - \int_{\partial B_0} \delta\bar{\boldsymbol{u}} \cdot \left(\bar{\boldsymbol{Q}} \cdot \boldsymbol{\nabla}_0\right) \cdot \bar{\boldsymbol{N}}\, d\partial B \\ &+ \int_{B_0} \delta\bar{\boldsymbol{u}} \cdot \bar{\boldsymbol{Q}} : (\boldsymbol{\nabla}_0 \otimes \boldsymbol{\nabla}_0)\, dB \quad \forall \delta\bar{\boldsymbol{u}} \in \mathrm{U}_c(B_0)\,. \end{aligned} \tag{9}$$

Following Mindlin's theory [16], the gradient is decomposed into a surface gradient $\overset{s}{\boldsymbol{\nabla}}_0$ and a normal part D such that

$$\boldsymbol{\nabla}_0(\cdot) = \overset{s}{\boldsymbol{\nabla}}_0(\cdot) + \bar{\boldsymbol{N}} D(\cdot)\,, \tag{10}$$

where $\overset{s}{\boldsymbol{\nabla}}_0 = \left(\boldsymbol{I} - \bar{\boldsymbol{N}} \otimes \bar{\boldsymbol{N}}\right) \cdot \boldsymbol{\nabla}_0$ and where $D = \bar{\boldsymbol{N}} \cdot \boldsymbol{\nabla}_0$.

Combining all these results, using the following relation [16]

$$\int_{\partial B_0} \overset{s}{\boldsymbol{\nabla}}_0 \cdot \left(\delta\bar{\boldsymbol{u}} \cdot \bar{\boldsymbol{Q}} \cdot \bar{\boldsymbol{N}}\right) d\partial B = \int_{\partial B_0} \left(\overset{s}{\boldsymbol{\nabla}}_0 \cdot \bar{\boldsymbol{N}}\right) \delta\bar{\boldsymbol{u}} \cdot \bar{\boldsymbol{Q}} : \left(\bar{\boldsymbol{N}} \otimes \bar{\boldsymbol{N}}\right) d\partial B\,, \tag{11}$$

and performing another integration by parts of the weak formulation (7) leads to the local strong form

$$\bar{\boldsymbol{B}} + \left(\bar{\boldsymbol{P}} - \bar{\boldsymbol{Q}} \cdot \boldsymbol{\nabla}_0\right) \cdot \boldsymbol{\nabla}_0 = \mathbf{0} \quad \forall \bar{\boldsymbol{X}} \in B_0\,, \tag{12}$$

$$\left(\bar{\boldsymbol{P}} - \bar{\boldsymbol{Q}} \cdot \boldsymbol{\nabla}_0\right) \cdot \bar{\boldsymbol{N}} + \left(\bar{\boldsymbol{Q}} \cdot \bar{\boldsymbol{N}}\right) \cdot \left(\bar{\boldsymbol{N}}\, \overset{s}{\boldsymbol{\nabla}}_0 \cdot \bar{\boldsymbol{N}} - \overset{s}{\boldsymbol{\nabla}}_0\right) = \bar{\boldsymbol{T}}^0 \quad \forall \bar{\boldsymbol{X}} \in \partial_N B_0\,, \tag{13}$$

$$\bar{\boldsymbol{Q}} : \left(\bar{\boldsymbol{N}} \otimes \bar{\boldsymbol{N}}\right) = \bar{\boldsymbol{R}}^0 \quad \forall \bar{\boldsymbol{X}} \in \partial_M B_0\,. \tag{14}$$

In these equations, $\hat{\boldsymbol{P}} = \left(\bar{\boldsymbol{P}} - \bar{\boldsymbol{Q}} \cdot \boldsymbol{\nabla}_0\right)$ is the effective stress, $\bar{\boldsymbol{T}} = \left(\bar{\boldsymbol{P}} - \bar{\boldsymbol{Q}} \cdot \boldsymbol{\nabla}_0\right) \cdot \bar{\boldsymbol{N}} + \left(\bar{\boldsymbol{Q}} \cdot \bar{\boldsymbol{N}}\right) \cdot \left(\bar{\boldsymbol{N}}\, \overset{s}{\boldsymbol{\nabla}}_0 \cdot \bar{\boldsymbol{N}} - \overset{s}{\boldsymbol{\nabla}}_0\right)$ is the effective surface traction and $\bar{\boldsymbol{R}} = \bar{\boldsymbol{Q}} : \left(\bar{\boldsymbol{N}} \otimes \bar{\boldsymbol{N}}\right)$ is the double surface traction.

In order to complete the problem stated by Eqs. (12) to (14), a material constitutive law is required. Therefore, a general form of the constitutive law relating the first Piola-Kirchhoff $\bar{\boldsymbol{P}}$ and the higher–order stress $\bar{\boldsymbol{Q}}$ to the history of the deformation gradient $\bar{\boldsymbol{F}}$ and of its gradient $\bar{\boldsymbol{G}}$ is supposed to be known

$$\bar{\boldsymbol{P}}(t) = \mathfrak{F}^{\bar{P}}\left\{\bar{\boldsymbol{F}}(\tau), \bar{\boldsymbol{G}}(\tau), \tau \in [0\ t]\right\} \text{ and} \tag{15}$$

$$\bar{\boldsymbol{Q}}(t) = \mathfrak{F}^{\bar{Q}}\left\{\bar{\boldsymbol{F}}(\tau), \bar{\boldsymbol{G}}(\tau), \tau \in [0\ t]\right\}. \tag{16}$$

Although some constitutive laws have explicit expressions for these relations, the purpose of this work is to obtain them from the resolution of the micro-scale problem.

2.2. Problem at the microscopic scale

The microscopic structure is characterized by the representative volume element (RVE) whose reference configuration is V_0 and whose external boundary is ∂V_0. Contrarily to the macroscopic problem where the gradient of the deformation gradient appears, the microscopic problem obeys to the classical continuum. In the absence of body forces, the equilibrium state equation is given by

$$\boldsymbol{P} \cdot \boldsymbol{\nabla}_0 = \mathbf{0} \qquad \forall \boldsymbol{X} \in V_0\,, \tag{17}$$

where $\boldsymbol{P}$ is the first Piola–Kirchhoff stress tensor at point $\boldsymbol{X}$. The microscopic boundary conditions are related to the macroscopic kinematic quantities, which are the macroscopic deformation gradient $\bar{\boldsymbol{F}}$ and its gradient $\bar{\boldsymbol{G}}$. These boundary conditions are given in [8] and are formulated in terms of the microscopic displacement fluctuation field $\boldsymbol{\omega}$ as

$$\int_{\partial V_0} \boldsymbol{\omega} \otimes \boldsymbol{N}\, d\partial V = \boldsymbol{0}, \text{ and} \tag{18}$$

$$\int_{\partial V_0} \boldsymbol{\omega} \otimes \boldsymbol{N} \otimes \boldsymbol{X}\, d\partial V = \boldsymbol{0}, \tag{19}$$

where the microscopic displacement fluctuation field $\boldsymbol{\omega}$ is defined as

$$\boldsymbol{\omega} = \boldsymbol{u} - \left(\bar{\boldsymbol{F}} - \boldsymbol{I}\right) \cdot \boldsymbol{X} - \frac{1}{2}\bar{\boldsymbol{G}} : (\boldsymbol{X} \otimes \boldsymbol{X}) \,. \tag{20}$$

In this study, the RVE geometry is restricted to a cube for 3–dimensional problems or to a square for 2–dimensional problems. To apply the periodic boundary condition in terms of the fluctuation field $\boldsymbol{\omega}$ on the RVE boundary ∂V_0, this one is divided into the positive part ∂V_0^+ and into the negative part ∂V_0^- such that

$$\partial V_0^+ \cup \partial V_0^- = \partial V_0 \,, \tag{21}$$

$$\partial V_0^+ \cap \partial V_0^- = \emptyset, \text{ and} \tag{22}$$

$$\boldsymbol{N}(\boldsymbol{X}^+) = -\boldsymbol{N}(\boldsymbol{X}^-) \quad \forall \boldsymbol{X}^+ \in \partial V_0^+ \text{ and matching } \boldsymbol{X}^- \in \partial V_0^- \,. \tag{23}$$

Using this boundary partition, the periodic condition

$$\boldsymbol{\omega}(\boldsymbol{X}^+) = \boldsymbol{\omega}(\boldsymbol{X}^-) \quad \forall \boldsymbol{X}^+ \in \partial V_0^+ \text{ and matching } \boldsymbol{X}^- \in \partial V_0^- \,, \tag{24}$$

satisfies automatically the first constraint (18). Moreover, because of the RVE shape

$$\boldsymbol{X}^+ - \boldsymbol{X}^- = -\|\boldsymbol{X}^+ - \boldsymbol{X}^-\| \boldsymbol{N}(\boldsymbol{X}^-) \,, \tag{25}$$

and combining Eqs. (23), (24) and (25), the second constraint (19) becomes

$$\int_{\partial V_0^-} \boldsymbol{\omega} \otimes \boldsymbol{N} \otimes \boldsymbol{N}\, d\partial V = \boldsymbol{0} \,. \tag{26}$$

On each surface S of the negative part of the RVE boundary, the normal $\boldsymbol{N}$ is constant and the condition

$$\int_{S \in \partial V_0^-} \boldsymbol{\omega}\, d\partial V = \boldsymbol{0}, \tag{27}$$

is chosen to satisfy Eq. (26). Finally, Eqs. (24) and (27) define the periodic boundary condition for the microscopic boundary value problem.

The determination of the macroscopic stresses (first Piola–Kirchhoff stress $\bar{\boldsymbol{P}}$ and higher–order stress $\bar{\boldsymbol{Q}}$) is based on the Hill–Mandel macro–homogeneity condition. This condition requires the energy consistency condition to be satisfied during the scale transition. In the context of the high–order continuum, this condition can be extended as follows

$$\bar{\boldsymbol{P}} : \delta\bar{\boldsymbol{F}} + \bar{\boldsymbol{Q}} \vdots \delta\bar{\boldsymbol{G}} = \frac{1}{V_0} \int_{V_0} \boldsymbol{P} : \delta\boldsymbol{F}\, dV \,, \tag{28}$$

where V_0 is the volume of the RVE, and where the variation of the microscopic deformation gradient is obtained from

Eq. (20) as being

$$\delta \boldsymbol{F} = \delta \bar{\boldsymbol{F}} + \delta \bar{\boldsymbol{G}} \cdot \boldsymbol{X} + \delta \boldsymbol{\omega} \otimes \boldsymbol{\nabla}_0 \,. \tag{29}$$

As $\delta \bar{\boldsymbol{F}}$ and $\delta \bar{\boldsymbol{G}}$ are arbitrary, the macroscopic stress and the macroscopic higher–order stress tensors can be expressed using Eqs. (28) and (29) from the microscopic volume integrals

$$\bar{\boldsymbol{P}} = \frac{1}{V_0} \int_{V_0} \boldsymbol{P}\, dV \text{ and } , \tag{30}$$

$$\bar{\boldsymbol{Q}} = \frac{1}{2V_0} \int_{V_0} \left[\boldsymbol{P} \otimes \boldsymbol{X} + (\boldsymbol{P} \otimes \boldsymbol{X})^{RC} \right] dV \,, \tag{31}$$

where $A^{RC}_{ijk} = A_{ikj}$ is the right transpose of any third order tensor $\boldsymbol{A}$, and where the remaining term

$$\int_{V_0} \boldsymbol{P} : (\delta \boldsymbol{\omega} \otimes \boldsymbol{\nabla}_0)\; dV = 0 \,, \tag{32}$$

which corresponds to the Hill–Mandel condition, must be satisfied. The volume integrals (30) to (32) can be transformed into surface integrals by using Eq. (17), which yields

$$\bar{\boldsymbol{P}} = \frac{1}{V_0} \int_{\partial V_0} \boldsymbol{t} \otimes \boldsymbol{X}\, d\partial V \,, \tag{33}$$

$$\bar{\boldsymbol{Q}} = \frac{1}{2V_0} \int_{\partial V_0} \boldsymbol{t} \otimes \boldsymbol{X} \otimes \boldsymbol{X}\, d\partial V \,, \tag{34}$$

and the Hill–Mandel condition

$$\int_{\partial V_0} \boldsymbol{t} \cdot \delta \boldsymbol{\omega}\, d\partial V = 0 \,. \tag{35}$$

In these relations, $\boldsymbol{t} = \boldsymbol{P} \cdot \boldsymbol{N}$ is the traction per unit reference surface.

The material behavior of each microscopic constituent α is described by its constitutive law. The general history dependent strain–stress relationship is specified by

$$\boldsymbol{P}(t) = \mathfrak{F}^{\alpha} \left\{ \boldsymbol{F}(\tau) \,,\;\; \tau \in [0 \;\; t] \right\} \,. \tag{36}$$

Finally, the microscopic boundary value problem is solved by seeking the solution of the equilibrium state equation (17) with the constraints (24) and (27) and with the constitutive law (36). Equation (35) is satisfied automatically if the periodic constraints (24) and (27) are satisfied either by using the constraint elimination method or by using the Lagrange multipliers method, in which case the multipliers represent the boundary forces. In a finite element analysis, the discrete constraints created from these periodic boundary conditions are easily obtained when using conformal meshes [4, 7, 8, 9]. In a more general setting, the conformity of mesh distributions on opposite boundaries of the representative volume element cannot always be guaranteed, leading to a non–periodic mesh. In that case, the periodic boundary conditions can be enforced using the polynomial interpolation method [37]. More details on the periodic boundary conditions enforcement are given in Section 4.

3. Finite–element resolution at the macroscopic scale: Discontinuous Galerkin formulation

Solving directly the problem formulated by the set of Eqs. (12– 14) using the conventional displacement–based finite element framework requires at least C^1 interpolation shape functions, which implies the continuity of the displacement field and of its derivatives. An alternative is the use of the C^0/DG method proposed in [24, 25]. The advantage of this method is to consider only the displacement field as degrees of freedom, and the related problems

coming from the introduction of additional unknowns can be avoided. The linear elastic formulation developed in [24, 25] is extended to the finite strain case in this section.

3.1. Discontinuous Galerkin formulation

The body B_0 is approximated by a discretized body B_0^h containing the finite elements Ω_0^e, with $B_0 \approx B_0^h = \bigcup_e \bar{\Omega}_0^e$ where $\bar{\Omega}_0^e$ is the union of the open domain Ω_0^e with its boundary $\partial\Omega_0^e$. The boundary of $\partial\Omega_0^e$ can be common with the boundary ∂B_0^h (see Fig. 2) with

$$\partial\Omega_0^e \cup \partial_D B_0^h = \partial_D\Omega_0^e\,,\ \partial\Omega_0^e \cup \partial_N B_0^h = \partial_N\Omega_0^e\,,\ \partial\Omega_0^e \cup \partial_T B_0^h = \partial_T\Omega_0^e\,,\ \text{ and } \partial\Omega_0^e \cup \partial_M B_0^h = \partial_M\Omega_0^e\,. \tag{37}$$

The remaining part of $\partial\Omega_0^e$ is common with other finite elements, with

$$\partial\Omega_0^e \cup \partial_I B_0^h = \partial_I\Omega_0^e \text{ where } \partial_I B_0^h = \bigcup_e \partial\Omega_0^e \setminus \partial B_0^h\,. \tag{38}$$

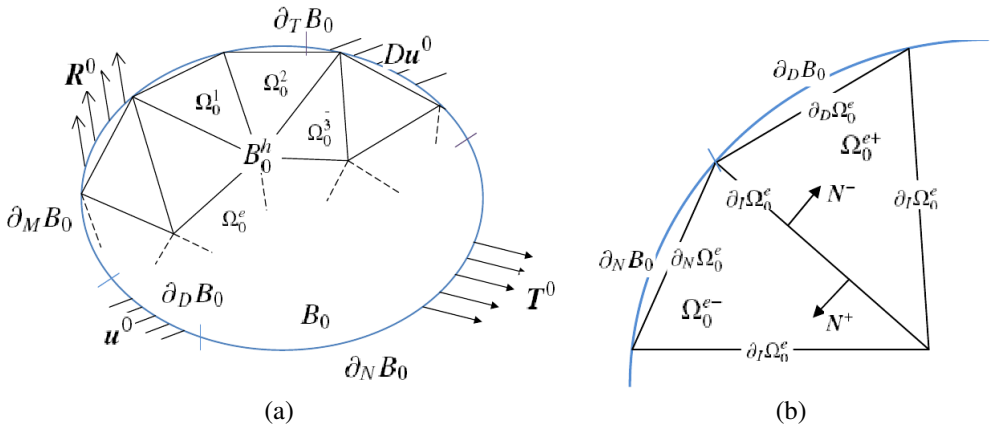

Figure 2: Description of the discretization B_0^h of B_0: (a) approximation B_0^h of the initial configuration B_0 and (b) details of two elements of the discretization B_0^h. The element boundary, the internal boundary and the outward normals between two elements are represented.

To find the solution of the finite element problem the manifold $\mathbb{P}^k$, which is the space of polynomial functions of order up to k with support in Ω_0^e, is used to approximate the displacement field within one element. Using the EDG method, these spaces are similar to the conventional finite element spaces, which satisfy the C^0 continuity condition, and allows for the jump of derivatives. When considering the FDG method these spaces differ from the conventional finite element spaces as they allows for the jump discontinuities for both the function value and the function derivatives at inter–element boundaries. This polynomial approximation leads to the definition of the displacement manifold and of its constrained counterpart

$$\mathrm{U}_{\mathrm{h}}^k = \left\{\bar{\boldsymbol{u}}^h \in \mathbf{L}^2\left(B_0^h\right) \mid \bar{\boldsymbol{u}}^h|_{\Omega_0^e} \in \mathbb{P}^k \ \ \forall\Omega_0^e \in B_0^h\right\} \text{ and} \tag{39}$$

$$\mathrm{U}_{\mathrm{hc}}^k = \left\{\delta\bar{\boldsymbol{u}} \in \mathrm{U}_{\mathrm{h}}^k \mid \delta\bar{\boldsymbol{u}}|_{\partial_D B_0} = 0\right\}\,. \tag{40}$$

for the FDG framework. The EDG formulation can be easily deduced by defining

$$\mathrm{U}_{\mathrm{h}}^k = \left\{\bar{\boldsymbol{u}}^h \in \mathbf{H}^1\left(B_0^h\right) \mid \bar{\boldsymbol{u}}^h|_{\Omega_0^e} \in \mathbb{P}^k \ \ \forall\Omega_0^e \in B_0^h\right\}\,, \tag{41}$$

in which cases the discontinuities in $\bar{\boldsymbol{u}}^h$ and $\delta\bar{\boldsymbol{u}}$ simply vanish from the formulation.

The aim of this section is to establish the weak form (7) for an approximation $\bar{\boldsymbol{u}}^h \in \mathrm{U}_{\mathrm{h}}^k$ of the exact solution $\bar{\boldsymbol{u}} \in \mathbf{H}^4$. This leads to a DG formulation of the weak formulation of the second gradient problem. For this purpose, starting

from the strong form (12), the problem can be stated as finding $\bar{\boldsymbol{u}}^h \in \mathrm{U}_{\mathrm{h}}^k$ such that

$$\sum_e \int_{\Omega_0^e} \left\{ \bar{B}_i + \frac{\partial}{\partial \bar{X}_j} \left[\bar{P}_{ij}\left(\bar{\boldsymbol{u}}^h\right) - \frac{\partial \bar{Q}_{ijk}\left(\bar{\boldsymbol{u}}^h\right)}{\partial X_k} \right] \right\} \delta\bar{u}_i \, dB = 0 \qquad \forall \delta\bar{\boldsymbol{u}} \in \mathrm{U}_{\mathrm{h}c}^k \,. \tag{42}$$

Applying the integrations by parts and the Gauss theorem leads to

$$\begin{aligned} &\sum_e \int_{\Omega_0^e} \bar{B}_i \delta\bar{u}_i \, dB - \sum_e \int_{\Omega_0^e} \bar{P}_{ij}\left(\bar{\boldsymbol{u}}^h\right) \frac{\partial \delta\bar{u}_i}{\partial \bar{X}_j} \, dB - \sum_e \int_{\Omega_0^e} \bar{Q}_{ijk}\left(\bar{\boldsymbol{u}}^h\right) \frac{\partial^2 \delta\bar{u}_i}{\partial \bar{X}_j \partial \bar{X}_k} \, dB + \\ &\sum_e \int_{\partial\Omega_0^e} \bar{N}_j \left\{ \left[\bar{P}_{ij}\left(\bar{\boldsymbol{u}}^h\right) - \frac{\partial \bar{Q}_{ijk}\left(\bar{\boldsymbol{u}}^h\right)}{\partial \bar{X}_k} \right] \delta\bar{u}_i + \bar{Q}_{ijk}\left(\bar{\boldsymbol{u}}^h\right) \frac{\partial \delta\bar{u}_i}{\partial \bar{X}_k} \right\} d\partial B = 0 \qquad \forall \delta\bar{\boldsymbol{u}} \in \mathrm{U}_{\mathrm{h}c}^k \,. \end{aligned} \tag{43}$$

Note that the displacement gradients $\delta\bar{\boldsymbol{u}} \otimes \bar{\boldsymbol{\nabla}}_0$ are discontinuous across the element boundaries. The use of the continuous or discontinuous displacement $\delta\bar{\boldsymbol{u}}$ field depends on the use of the EDG method or of the FDG method respectively. In this section the formulation is developed in the most general case of the FDG formulation, and the surface terms imposing weakly continuous properties related to $\delta\bar{\boldsymbol{u}}$ are to be ignored in the case of the EDG formulation.

Because of the existence of discontinuities, the jump $[\![\bullet]\!]$ and mean $\langle\bullet\rangle$ operators are defined on the space of the trace $\mathbf{TR}\left(\partial_I B_0^h\right) = \prod_e \mathbf{L}^2\left(\partial_I \Omega^e\right)$ of tensors (from first up to sixth order) that can take multiple values on this boundary, with

$$[\![\bullet]\!] = \bullet^+ - \bullet^- \; : \; \mathbf{TR}\left(\partial_I B_0^h\right) \to \mathbf{L}^2\left(\partial_I B_0^h\right) \text{, and} \tag{44}$$

$$\langle\bullet\rangle = \frac{1}{2}\left(\bullet^+ + \bullet^-\right) \; : \; \mathbf{TR}\left(\partial_I B_0^h\right) \to \mathbf{L}^2\left(\partial_I B_0^h\right) . \tag{45}$$

In these relations the bullets represent a generic field with

$$\bullet^+ = \lim_{\varepsilon \to 0^+} \bullet\left(\bar{\boldsymbol{X}} + \varepsilon \bar{\boldsymbol{N}}^-\right) \text{ and } \bullet^- = \lim_{\varepsilon \to 0^+} \bullet\left(\bar{\boldsymbol{X}} - \varepsilon \bar{\boldsymbol{N}}^-\right) , \tag{46}$$

where $\bar{\boldsymbol{N}}^-$ is defined as the reference outward unit normal of the minus element Ω_0^e whereas $\bar{\boldsymbol{N}}^+$ is the reference outward unit normal of its neighboring element. Clearly,

$$\bar{\boldsymbol{N}}^- = -\bar{\boldsymbol{N}}^+ \quad \forall \bar{\boldsymbol{X}} \in \partial_I B_0^h \,. \tag{47}$$

Note that if definition (44) of the jump operator depends on the choice of the + and − elements, the formulation becomes consistent and independent of this choice when using this jump in combination with the outward unit normal $\bar{\boldsymbol{N}}^-$. From these definitions the surface terms in Eq. (43) can be rewritten as

$$\begin{aligned} &\sum_e \int_{\partial\Omega_0^e} \bar{N}_j \left\{ \left[\bar{P}_{ij}\left(\bar{\boldsymbol{u}}^h\right) - \frac{\partial \bar{Q}_{ijk}\left(\bar{\boldsymbol{u}}^h\right)}{\partial \bar{X}_k} \right] \delta\bar{u}_i + \bar{Q}_{ijk}\left(\bar{\boldsymbol{u}}^h\right) \frac{\partial \delta\bar{u}_i}{\partial \bar{X}_k} \right\} d\partial B = \\ &\int_{\partial B_0^h} \bar{N}_j \left\{ \left[\bar{P}_{ij}\left(\bar{\boldsymbol{u}}^h\right) - \frac{\partial \bar{Q}_{ijk}\left(\bar{\boldsymbol{u}}^h\right)}{\partial \bar{X}_k} \right] \delta\bar{u}_i + \bar{Q}_{ijk}\left(\bar{\boldsymbol{u}}^h\right) \frac{\partial \delta\bar{u}_i}{\partial \bar{X}_k} \right\} d\partial B \\ - \int_{\partial_I B_0^h} \bar{N}_j^- \left[\!\!\left[\hat{P}_{ij}\left(\bar{\boldsymbol{u}}^h\right) \delta\bar{u}_i \right]\!\!\right] d\partial B - &\int_{\partial_I B_0^h} \bar{N}_j^- \left[\!\!\left[\bar{Q}_{ijk}\left(\bar{\boldsymbol{u}}^h\right) \frac{\partial \delta\bar{u}_i}{\partial \bar{X}_k} \right]\!\!\right] d\partial B \qquad \forall \delta\bar{\boldsymbol{u}} \in \mathrm{U}_{\mathrm{h}c}^k \,, \end{aligned} \tag{48}$$

where the definition of the effective stress $\hat{\boldsymbol{P}}\left(\bar{\boldsymbol{u}}^h\right)$ reads

$$\hat{P}_{ij}\left(\bar{\boldsymbol{u}}^h\right) = \bar{P}_{ij}\left(\bar{\boldsymbol{u}}^h\right) - \frac{\partial \bar{Q}_{ijk}\left(\bar{\boldsymbol{u}}^h\right)}{\partial \bar{X}_k}\,. \tag{49}$$

The main idea of the discontinuous Galerkin method is to address the contribution of the inter–element discontinuity terms by introducing numerical fluxes $\boldsymbol{h}\left(\hat{\boldsymbol{P}}^+, \hat{\boldsymbol{P}}^-, \bar{\boldsymbol{N}}^-\right)$ and $\boldsymbol{H}\left(\bar{\boldsymbol{Q}}^+, \bar{\boldsymbol{Q}}^-, \bar{\boldsymbol{N}}^-\right)$ dependent on the limit values on the surface in the neighboring elements, such that

$$\int_{\partial_I B_0^h} \bar{N}_j^- \left[\!\left[\hat{P}_{ij}\left(\bar{\boldsymbol{u}}^h\right)\delta\bar{u}_i\right]\!\right] d\partial B \simeq \int_{\partial_I B_0^h} [\![\delta\bar{u}_i]\!]\, h_i\left(\hat{\boldsymbol{P}}^+, \hat{\boldsymbol{P}}^-, \bar{\boldsymbol{N}}^-\right) d\partial B\,, \text{ and} \tag{50}$$

$$\int_{\partial_I B_0^h} \bar{N}_j^- \left[\!\left[\bar{Q}_{ijk}\left(\bar{\boldsymbol{u}}^h\right)\frac{\partial\delta\bar{u}_i}{\partial\bar{X}_k}\right]\!\right] d\partial B \simeq \int_{\partial_I B_0^h} \left[\!\left[\frac{\partial\delta\bar{u}_i}{\partial\bar{X}_j}\right]\!\right] H_{ij}\left(\bar{\boldsymbol{Q}}^+, \bar{\boldsymbol{Q}}^-, \bar{\boldsymbol{N}}^-\right) d\partial B\,. \tag{51}$$

In principle there is a significant freedom in the choice of these fluxes but only a few expressions lead to stable and consistent formulations. These expressions have to verify the consistency conditions

$$\boldsymbol{h}\left(\hat{\boldsymbol{P}}, \hat{\boldsymbol{P}}, \bar{\boldsymbol{N}}\right) = \hat{\boldsymbol{P}}\cdot\bar{\boldsymbol{N}} \text{ and } \boldsymbol{h}\left(\hat{\boldsymbol{P}}^+, \hat{\boldsymbol{P}}^-, \bar{\boldsymbol{N}}^-\right) = -\boldsymbol{h}\left(\hat{\boldsymbol{P}}^-, \hat{\boldsymbol{P}}^+, \bar{\boldsymbol{N}}^+\right), \text{ and} \tag{52}$$

$$\boldsymbol{H}\left(\bar{\boldsymbol{Q}}, \bar{\boldsymbol{Q}}, \bar{\boldsymbol{N}}\right) = \bar{\boldsymbol{Q}}\cdot\bar{\boldsymbol{N}} \text{ and } \boldsymbol{H}\left(\bar{\boldsymbol{Q}}^+, \bar{\boldsymbol{Q}}^-, \bar{\boldsymbol{N}}^-\right) = -\boldsymbol{H}\left(\bar{\boldsymbol{Q}}^-, \bar{\boldsymbol{Q}}^+, \bar{\boldsymbol{N}}^+\right), \tag{53}$$

where $\hat{\boldsymbol{P}}$ and $\bar{\boldsymbol{Q}}$ are the exact solutions. In this paper, the following expressions are adopted

$$h_i\left(\hat{\boldsymbol{P}}^+, \hat{\boldsymbol{P}}^-, \bar{\boldsymbol{N}}^-\right) = \left\langle\hat{P}_{ij}\right\rangle\bar{N}_j^- + \frac{1}{2}\bar{N}_j^-\left\langle\frac{\beta^P}{h^s}C^0_{ijkl}\right\rangle[\![\bar{u}_k]\!]\,\bar{N}_l^-\,, \text{ and} \tag{54}$$

$$H_{ij}\left(\bar{\boldsymbol{Q}}^+, \bar{\boldsymbol{Q}}^-, \bar{\boldsymbol{N}}^-\right) = \left\langle\bar{Q}_{ijk}\right\rangle\bar{N}_k^- + \frac{1}{2}\bar{N}_k^-\left\langle\frac{\beta^Q}{h^s}\mathcal{J}^0_{ijkpqr}\right\rangle\left[\!\left[\frac{\partial\bar{u}_p}{\partial\bar{X}_q}\right]\!\right]\bar{N}_r^-\,, \tag{55}$$

where β^P and β^Q are the user stabilization parameters, h^s is the characteristic mesh size of the problem, $\boldsymbol{C}^0 = \frac{\partial\bar{\boldsymbol{P}}}{\partial\bar{\boldsymbol{F}}}$ is the tangent operator of the constitutive law $\bar{\boldsymbol{P}}$ in terms of the deformation gradient $\bar{\boldsymbol{F}}$, and where $\boldsymbol{\mathcal{J}}^0 = \frac{\partial\bar{\boldsymbol{Q}}}{\partial\bar{\boldsymbol{G}}}$ is the higher–order tangent operator of the constitutive law $\bar{\boldsymbol{Q}}$ in terms of the higher–order gradient $\bar{\boldsymbol{G}}$. As the second part of the fluxes ensures the stability of the method $\boldsymbol{C}^0$ and $\boldsymbol{\mathcal{J}}^0$ can be chosen constant during the simulations and are evaluated at the zero–strain state, which explains the superscript 0. Using these tensors has two advantages. On the one hand, it avoids evaluating their derivatives during the Newton–Raphson iterations, and on the other hand, it prevents the stability terms to vanish in case of material softening.

Using Eqs. (48) to (51), the weak form (43) becomes finding $\bar{\boldsymbol{u}}^h \in \mathrm{U}^k_{\mathrm{h}}$ such that

$$\begin{aligned}
&\int_{B_0^h} \bar{B}_i\delta\bar{u}_i\,dB - \int_{B_0^h}\bar{P}_{ij}\left(\bar{\boldsymbol{u}}^h\right)\frac{\partial\delta\bar{u}_i}{\partial\bar{X}_j}\,dB - \int_{B_0^h}\bar{Q}_{ijk}\left(\bar{\boldsymbol{u}}^h\right)\frac{\partial^2\delta\bar{u}_i}{\partial\bar{X}_j\partial\bar{X}_k}\,dB \\
&\quad + \int_{\partial B_0^h}\bar{N}_j\left\{\left[\bar{P}_{ij}\left(\bar{\boldsymbol{u}}^h\right) - \frac{\partial\bar{Q}_{ijk}\left(\bar{\boldsymbol{u}}^h\right)}{\partial\bar{X}_k}\right]\delta\bar{u}_i + \bar{Q}_{ijk}\left(\bar{\boldsymbol{u}}^h\right)\frac{\partial\delta\bar{u}_i}{\partial\bar{X}_k}\right\} d\partial B \\
-\int_{\partial_I B_0^h}[\![\delta\bar{u}_i]\!]\,h_i\left(\hat{\boldsymbol{P}}^+, \hat{\boldsymbol{P}}^-, \bar{\boldsymbol{N}}^-\right) d\partial B - \int_{\partial_I B_0^h}\left[\!\left[\frac{\partial\delta\bar{u}_i}{\partial\bar{X}_j}\right]\!\right]H_{ij}\left(\bar{\boldsymbol{Q}}^+, \bar{\boldsymbol{Q}}^-, \bar{\boldsymbol{N}}^-\right) d\partial B = 0 \qquad \forall\delta\bar{\boldsymbol{u}} \in \mathrm{U}^k_{\mathrm{h}c}\,.
\end{aligned} \tag{56}$$

This last equation can be simplified by using Eqs. (10) and (11), yielding

$$\begin{aligned}
&\int_{B_0^h} \bar{B}_i \delta\bar{u}_i \, dB - \int_{B_0^h} \bar{P}_{ij}\left(\bar{\boldsymbol{u}}^h\right) \frac{\partial \delta\bar{u}_i}{\partial \bar{X}_j} \, dB - \int_{B_0^h} \bar{Q}_{ijk}\left(\bar{\boldsymbol{u}}^h\right) \frac{\partial^2 \delta\bar{u}_i}{\partial \bar{X}_j \partial \bar{X}_k} \, dB \\
&+ \int_{\partial_N B_0^h} \left\{ \bar{N}_j \left[\bar{P}_{ij}\left(\bar{\boldsymbol{u}}^h\right) - \frac{\partial \bar{Q}_{ijk}\left(\bar{\boldsymbol{u}}^h\right)}{\partial \bar{X}_k} \right] + \frac{\partial^s \bar{N}_l}{\partial \bar{X}_l} \bar{Q}_{ijk} \bar{N}_j \bar{N}_k - \frac{\partial^s \bar{Q}_{ijk} \bar{N}_j}{\partial \bar{X}_k} \right\} \delta\bar{u}_i \, d\partial B \\
&+ \int_{\partial_T B_0^h} \bar{Q}_{ijk} \bar{N}_j \bar{N}_k D\delta\bar{u}_i \, d\partial B + \int_{\partial_M B_0^h} \bar{Q}_{ijk} \bar{N}_j \bar{N}_k D\delta\bar{u}_i \, d\partial B \\
&- \int_{\partial_I B_0^h} [\![\delta\bar{u}_i]\!] \, h_i\left(\hat{\boldsymbol{P}}^+, \hat{\boldsymbol{P}}^-, \bar{\boldsymbol{N}}^-\right) d\partial B - \int_{\partial_I B_0^h} \left[\!\!\left[\frac{\partial \delta\bar{u}_i}{\partial \bar{X}_j} \right]\!\!\right] H_{ij}\left(\bar{\boldsymbol{Q}}^+, \bar{\boldsymbol{Q}}^-, \bar{\boldsymbol{N}}^-\right) d\partial B = 0 \qquad \forall \delta\bar{\boldsymbol{u}} \in \mathrm{U}_{\mathrm{h}c}^k \,,
\end{aligned} \tag{57}$$

or again, using the boundary conditions (13) and (14),

$$\begin{aligned}
&\int_{B_0^h} \bar{B}_i \delta\bar{u}_i \, dB - \int_{B_0^h} \bar{P}_{ij}\left(\bar{\boldsymbol{u}}^h\right) \frac{\partial \delta\bar{u}_i}{\partial \bar{X}_j} \, dB - \int_{B_0^h} \bar{Q}_{ijk}\left(\bar{\boldsymbol{u}}^h\right) \frac{\partial^2 \delta\bar{u}_i}{\partial \bar{X}_j \partial \bar{X}_k} \, dB \\
&+ \int_{\partial_N B_0^h} \bar{T}_i^0 \delta\bar{u}_i \, d\partial B + \int_{\partial_M B_0^h} \bar{R}_i^0 D\delta\bar{u}_i \, d\partial B + \int_{\partial_T B_0^h} \bar{Q}_{ijk} \bar{N}_j \bar{N}_k D\delta\bar{u}_i \, d\partial B \\
&- \int_{\partial_I B_0^h} [\![\delta\bar{u}_i]\!] \, h_i\left(\hat{\boldsymbol{P}}^+, \hat{\boldsymbol{P}}^-, \bar{\boldsymbol{N}}^-\right) d\partial B - \int_{\partial_I B_0^h} \left[\!\!\left[\frac{\partial \delta\bar{u}_i}{\partial \bar{X}_j} \right]\!\!\right] H_{ij}\left(\bar{\boldsymbol{Q}}^+, \bar{\boldsymbol{Q}}^-, \bar{\boldsymbol{N}}^-\right) d\partial B = 0 \qquad \forall \delta\bar{\boldsymbol{u}} \in \mathrm{U}_{\mathrm{h}c}^k \,.
\end{aligned} \tag{58}$$

The weak enforcement of $\bar{\boldsymbol{u}}^h$ continuity on $\partial_I B_0^h$ and the symmetrization of the linearized formulation can be obtained by weakly constraining the displacement jump:

$$\int_{\partial_I B_0^h} \left[\!\!\left[\bar{u}_i^h \right]\!\!\right] h_i\left(\hat{\boldsymbol{P}}^+\left(\delta\bar{\boldsymbol{u}}\right), \hat{\boldsymbol{P}}^-\left(\delta\bar{\boldsymbol{u}}\right), \bar{\boldsymbol{N}}^-\right) d\partial B = 0 \,. \tag{59}$$

Similarly, it comes for $\bar{\boldsymbol{u}}^h \otimes \boldsymbol{\nabla}_0$:

$$\int_{\partial_I B_0^h} \left[\!\!\left[\frac{\partial \bar{u}_i^h}{\partial \bar{X}_j} \right]\!\!\right] H_{ij}\left(\bar{\boldsymbol{Q}}^+\left(\delta\bar{\boldsymbol{u}}\right), \bar{\boldsymbol{Q}}^-\left(\delta\bar{\boldsymbol{u}}\right), \bar{\boldsymbol{N}}^-\right) d\partial B = 0 \,. \tag{60}$$

The boundary condition $D\bar{\boldsymbol{u}}^h = D\bar{\boldsymbol{u}}^0$ on $\partial_T B_0^h$ can also be weakly enforced. For this purpose, the jump and mean operator definitions are extended on $\partial_T B_0^h$ as

$$\left[\!\!\left[\bar{N}_j D\bar{u}_i \right]\!\!\right] = \bar{N}_j D\bar{u}_i^0 - \bar{N}_j D\bar{u}_i^h \,, \; \left[\!\!\left[\bar{N}_j D\delta\bar{u}_i \right]\!\!\right] = -\bar{N}_j D\delta\bar{u}_i \text{ and } \left\langle \bar{\boldsymbol{Q}} \right\rangle = \bar{\boldsymbol{Q}} \text{ on } \partial_T B_0^h \,. \tag{61}$$

Using the definition (55), the boundary term on $D\bar{\boldsymbol{u}}$ in Eq. (58) is approximated by

$$\int_{\partial_T B_0^h} \bar{Q}_{ijk} \bar{N}_j \bar{N}_k D\delta\bar{u}_i \, d\partial B \simeq - \int_{\partial_T B_0^h} \left[\!\!\left[\bar{N}_j D\delta\bar{u}_i \right]\!\!\right] H_{ij}\left(\bar{\boldsymbol{Q}}\left(\bar{\boldsymbol{u}}^h\right), \bar{\boldsymbol{Q}}\left(\bar{\boldsymbol{u}}^h\right), \bar{\boldsymbol{N}}^-\right) d\partial B \,, \tag{62}$$

while the weak enforcement of the boundary condition results in a new weak form

$$\int_{\partial_T B_0^h} \left[\!\!\left[\bar{N}_j D\bar{u}_i^h \right]\!\!\right] H_{ij}\left(\bar{\boldsymbol{Q}}\left(\delta\bar{\boldsymbol{u}}\right), \bar{\boldsymbol{Q}}\left(\delta\bar{\boldsymbol{u}}\right), \bar{\boldsymbol{N}}\right) d\partial B = 0 \,. \tag{63}$$

Using the Eqs. (58) to (63) leads to the discontinuous Galerkin formulation of the problem which is stated as

finding $\bar{\boldsymbol{u}}^h \in \mathrm{U}_{\mathrm{h}}^k$ such that

$$\begin{aligned}
&\int_{B_0^h} \bar{P}_{ij}\left(\bar{\boldsymbol{u}}^h\right) \frac{\partial \delta \bar{u}_i}{\partial \bar{X}_j}\, dB + \int_{B_0^h} \bar{Q}_{ijk}\left(\bar{\boldsymbol{u}}^h\right) \frac{\partial^2 \delta \bar{u}_i}{\partial \bar{X}_j \partial \bar{X}_k}\, dB + \\
&\int_{\partial_I B_0^h} [\![\delta \bar{u}_i]\!]\, h_i\left(\hat{\boldsymbol{P}}^+, \hat{\boldsymbol{P}}^-, \bar{\boldsymbol{N}}^-\right) d\partial B + \\
&\int_{\partial_I B_0^h} \left[\!\left[\bar{u}_i^h\right]\!\right] h_i\left(\hat{\boldsymbol{P}}^+\left(\delta\bar{\boldsymbol{u}}\right), \hat{\boldsymbol{P}}^-\left(\delta\bar{\boldsymbol{u}}\right), \bar{\boldsymbol{N}}^-\right) d\partial B + \\
&\int_{\partial_I B_0^h} \left[\!\left[\frac{\partial \delta \bar{u}_i}{\partial \bar{X}_j}\right]\!\right] H_{ij}\left(\bar{\boldsymbol{Q}}^+, \bar{\boldsymbol{Q}}^-, \bar{\boldsymbol{N}}^-\right) d\partial B + \\
&\int_{\partial_I B_0^h} \left[\!\left[\frac{\partial \bar{u}_i^h}{\partial \bar{X}_j}\right]\!\right] H_{ij}\left(\bar{\boldsymbol{Q}}^+\left(\delta\bar{\boldsymbol{u}}\right), \bar{\boldsymbol{Q}}^-\left(\delta\bar{\boldsymbol{u}}\right), \bar{\boldsymbol{N}}^-\right) d\partial B + \\
&\int_{\partial_T B_0^h} \left[\!\left[\bar{N}_j D\delta \bar{u}_i\right]\!\right] H_{ij}\left(\bar{\boldsymbol{Q}}\left(\bar{\boldsymbol{u}}^{\boldsymbol{h}}\right), \bar{\boldsymbol{Q}}\left(\bar{\boldsymbol{u}}^{\boldsymbol{h}}\right), \bar{\boldsymbol{N}}^-\right) d\partial B + \\
&\int_{\partial_T B_0^h} \left[\!\left[\bar{N}_j D\bar{u}_i^h\right]\!\right] H_{ij}\left(\bar{\boldsymbol{Q}}\left(\delta\bar{\boldsymbol{u}}\right), \bar{\boldsymbol{Q}}\left(\delta\bar{\boldsymbol{u}}\right), \bar{\boldsymbol{N}}\right) d\partial B = \\
&\int_{B_0^h} \bar{B}_i \delta \bar{u}_i\, dB + \int_{\partial_N B_0^h} \bar{T}_i^0 \delta \bar{u}_i\, d\partial B + \int_{\partial_M B_0^h} \bar{R}_i^0 D\delta \bar{u}_i\, d\partial B \qquad \forall \delta\bar{\boldsymbol{u}} \in \mathrm{U}_{\mathrm{h}c}^k\,.
\end{aligned} \tag{64}$$

It is clear that the treatment of the weak enforcement of high order boundary conditions is similar to the treatment of the weak enforcement of the high order stress at inter–element boundaries. In what follows, it is assumed that there is no boundary condition on $\partial_T B_0$, leading to the assumption $\partial_M B_0 = \partial B_0$.

Using the fluxes (54) and (55), the weak form (64) can be rewritten as finding $\bar{\boldsymbol{u}}^h \in \mathrm{U}_{\mathrm{h}}^k$ such that

$$a\left(\bar{\boldsymbol{u}}^h, \delta\bar{\boldsymbol{u}}\right) = b\left(\delta\bar{\boldsymbol{u}}\right) \qquad \forall \delta\bar{\boldsymbol{u}} \in \mathrm{U}_{\mathrm{h}c}^k\,, \tag{65}$$

where

$$\begin{aligned}
a\left(\bar{\boldsymbol{u}}^h, \delta\bar{\boldsymbol{u}}\right) = &\sum_e \underbrace{\int_{\Omega_0^e} \bar{P}_{ij}\left(\bar{\boldsymbol{u}}^h\right) \frac{\partial \delta \bar{u}_i}{\partial \bar{X}_j}\, dB}_{a_{\mathrm{PF}}^e} + \sum_e \underbrace{\int_{\Omega_0^e} \bar{Q}_{ijk}\left(\bar{\boldsymbol{u}}^h\right) \frac{\partial^2 \delta \bar{u}_i}{\partial \bar{X}_j \partial \bar{X}_k}\, dB}_{a_{\mathrm{QG}}^e} + \\
&\sum_{s\in\partial_I B_0} \underbrace{\int_s [\![\delta \bar{u}_i]\!] \left\langle \hat{P}_{ij}\right\rangle \bar{N}_j^-\, d\partial B}_{a_{\mathrm{Ps}}^{\mathrm{I1}}} + \sum_{s\in\partial_I B_0} \underbrace{\int_s \left[\!\left[\bar{u}_i^h\right]\!\right] \left\langle \hat{P}_{ij}\left(\delta\bar{\boldsymbol{u}}\right)\right\rangle \bar{N}_j^-\, d\partial B}_{a_{\mathrm{Ps}}^{\mathrm{I2}}} + \\
&\sum_{s\in\partial_I B_0} \underbrace{\int_s \left[\!\left[\bar{u}_i^h\right]\!\right] \bar{N}_j^- \left\langle \frac{\beta^P}{h^s} C_{ijkl}^0\right\rangle [\![\delta \bar{u}_k]\!]\, \bar{N}_l^-\, d\partial B}_{a_{\mathrm{Ps}}^{\mathrm{I3}}} + \\
&\sum_{s\in\partial_I B_0} \underbrace{\int_s \left[\!\left[\frac{\partial \delta \bar{u}_i}{\partial \bar{X}_j}\right]\!\right] \left\langle \bar{Q}_{ijk}\right\rangle \bar{N}_k^-\, d\partial B}_{a_{\mathrm{Qs}}^{\mathrm{I1}}} + \sum_{s\in\partial_I B_0} \underbrace{\int_s \left[\!\left[\frac{\partial \bar{u}_i^h}{\partial \bar{X}_j}\right]\!\right] \left\langle \bar{Q}_{ijk}\left(\delta\bar{\boldsymbol{u}}\right)\right\rangle \bar{N}_k^-\, d\partial B}_{a_{\mathrm{Qs}}^{\mathrm{I2}}} + \\
&\sum_{s\in\partial_I B_0} \underbrace{\int_s \left[\!\left[\frac{\partial \bar{u}_i^h}{\partial \bar{X}_j}\right]\!\right] \bar{N}_k^- \left\langle \frac{\beta^Q}{h^s} \mathcal{J}_{ijkpqr}^0\right\rangle \left[\!\left[\frac{\partial \delta \bar{u}_p}{\partial \bar{X}_q}\right]\!\right] \bar{N}_j^-\, d\partial B}_{a_{\mathrm{Qs}}^{\mathrm{I3}}},
\end{aligned} \tag{66}$$

with

$$\begin{aligned}\hat{P}_{ij} &= \bar{P}_{ij} - \frac{\partial \bar{Q}_{ijk}}{\partial \bar{X}_k} = \bar{P}_{ij} - \frac{\partial \bar{Q}_{ijk}}{\partial \bar{F}_{pq}}\frac{\partial \bar{F}_{pq}}{\partial \bar{X}_k} - \frac{\partial \bar{Q}_{ijk}}{\partial \bar{G}_{pqr}}\frac{\partial \bar{G}_{pqr}}{\partial \bar{X}_k} \\ &= \bar{P}_{ij} - \mathcal{L}^{\bar{G}\bar{F}}_{ijkpq}\bar{G}_{pqk} - \mathcal{J}_{ijkpqr}\bar{K}_{pqrk}\,, \end{aligned} \tag{67}$$

and with

$$b\left(\delta\bar{\boldsymbol{u}}\right) = \int_{B_0^h} \bar{B}_i \delta\bar{u}_i \, dB + \int_{\partial_N B_0^h} \bar{T}_i^0 \delta\bar{u}_i \, d\partial B + \int_{\partial_M B_0^h} \bar{R}_i^0 D\delta\bar{u}_i \, d\partial B\,. \tag{68}$$

By analogy to what has been done for the stabilization part of the fluxes (54) and (55), we use the constant moduli when developing $\hat{P}_{ij}\left(\delta\bar{\boldsymbol{u}}\right)$ and $\bar{Q}_{ijk}\left(\delta\bar{\boldsymbol{u}}\right)$:

$$\hat{P}_{ij}\left(\delta\bar{\boldsymbol{u}}\right) = C^0_{ijkl}\frac{\partial\delta\bar{u}_k}{\partial\bar{X}_l} + \mathcal{L}^{\bar{F}\bar{G}0}_{ijklm}\frac{\partial^2\delta\bar{u}_k}{\partial\bar{X}_l\partial\bar{X}_m} - \mathcal{L}^{\bar{G}\bar{F}0}_{ijkpq}\frac{\partial^2\delta\bar{u}_p}{\partial\bar{X}_q\bar{X}_k} - \mathcal{J}^0_{ijkpqr}\frac{\partial^3\delta\bar{u}_p}{\partial\bar{X}_q\partial\bar{X}_r\partial\bar{X}_k} \text{ and} \tag{69}$$

$$\bar{Q}_{ijk}\left(\delta\bar{\boldsymbol{u}}\right) = \mathcal{J}^0_{ijkpqr}\frac{\partial^2\delta\bar{u}_p}{\partial\bar{X}_q\partial\bar{X}_r} + \mathcal{L}^{\bar{G}\bar{F}0}_{ijkpq}\frac{\partial\delta\bar{u}_p}{\partial\bar{X}_q}\,, \tag{70}$$

where $\boldsymbol{\mathcal{L}}^{\bar{F}\bar{G}} = \frac{\partial\bar{\boldsymbol{P}}}{\partial\bar{\boldsymbol{G}}}$.

The volume terms $a^e_{\mathrm{PF}}\left(\bar{\boldsymbol{u}}^h, \delta\bar{\boldsymbol{u}}\right)$ and $a^e_{\mathrm{QG}}\left(\bar{\boldsymbol{u}}^h, \delta\bar{\boldsymbol{u}}\right)$ in (66) correspond to the usual contributions of the deformation gradient and of its gradient to the material response. The surface terms $a^{\mathrm{I1}}_{\mathrm{Ps}}\left(\bar{\boldsymbol{u}}^h, \delta\bar{\boldsymbol{u}}\right)$, $a^{\mathrm{I2}}_{\mathrm{Ps}}\left(\bar{\boldsymbol{u}}^h, \delta\bar{\boldsymbol{u}}\right)$, $a^{\mathrm{I3}}_{\mathrm{Ps}}\left(\bar{\boldsymbol{u}}^h, \delta\bar{\boldsymbol{u}}\right)$, $a^{\mathrm{I1}}_{\mathrm{Qs}}\left(\bar{\boldsymbol{u}}^h, \delta\bar{\boldsymbol{u}}\right)$, $a^{\mathrm{I2}}_{\mathrm{Qs}}\left(\bar{\boldsymbol{u}}^h, \delta\bar{\boldsymbol{u}}\right)$ and $a^{\mathrm{I3}}_{\mathrm{Qs}}\left(\bar{\boldsymbol{u}}^h, \delta\bar{\boldsymbol{u}}\right)$ result from the discontinuities on the inter–element boundaries. They ensure the method consistency, the symmetric nature of the stiffness matrix of the linearized problem, and the method stability. Following classical DG demonstrations, e.g. [25, 26, 35], it can be shown that the non–linear formulation (65) is consistent and that its linearization is stable for β^P and β^Q larger than constants depending on the element polynomial approximation only.[1] Moreover the linearized problem has a convergence rate in the $\boldsymbol{H}^1$–norm, or energy–norm ,in $k-1$, if k is the degree of the polynomial approximation and where the energy–norm is given by

$$\begin{aligned}|||e|||^2 &= \sum_e \int_{\Omega_0^e} \left(\bar{\boldsymbol{u}}\otimes\boldsymbol{\nabla}_0 - \bar{\boldsymbol{u}}^{\mathrm{exact}}\otimes\boldsymbol{\nabla}_0\right) : \boldsymbol{C} : \left(\bar{\boldsymbol{u}}\otimes\boldsymbol{\nabla}_0 - \bar{\boldsymbol{u}}^{\mathrm{exact}}\otimes\boldsymbol{\nabla}_0\right) dB \\ &+ \sum_e \int_{\Omega_0^e} \left(\bar{\boldsymbol{u}}\otimes\boldsymbol{\nabla}_0\otimes\boldsymbol{\nabla}_0 - \bar{\boldsymbol{u}}^{\mathrm{exact}}\otimes\boldsymbol{\nabla}_0\otimes\boldsymbol{\nabla}_0\right) \vdots \boldsymbol{\mathcal{J}} \vdots \left(\bar{\boldsymbol{u}}\otimes\boldsymbol{\nabla}_0\otimes\boldsymbol{\nabla}_0 - \bar{\boldsymbol{u}}^{\mathrm{exact}}\otimes\boldsymbol{\nabla}_0\otimes\boldsymbol{\nabla}_0\right) dB \\ &+ \sum_s \int_{\partial\Omega_0^e} \left(\llbracket\bar{\boldsymbol{u}}\rrbracket\otimes\bar{\boldsymbol{N}}\right) : \left\langle\frac{\beta^P\boldsymbol{C}^0}{h^s}\right\rangle : \left(\llbracket\bar{\boldsymbol{u}}\rrbracket\otimes\bar{\boldsymbol{N}}\right) d\partial B \\ &+ \sum_s \int_{\partial\Omega_0^e} \left(\llbracket\bar{\boldsymbol{u}}\otimes\boldsymbol{\nabla}_0\rrbracket\otimes\bar{\boldsymbol{N}}\right) \vdots \left\langle\frac{\beta^Q\boldsymbol{\mathcal{J}}^0}{h^s}\right\rangle \vdots \left(\llbracket\bar{\boldsymbol{u}}\otimes\boldsymbol{\nabla}_0\rrbracket\otimes\bar{\boldsymbol{N}}\right) d\partial B\,. \end{aligned} \tag{71}$$

The convergence rate in the $\boldsymbol{L}^2$–norm is 2 for quadratic elements and $k+1$ for at least cubic polynomial approximations, see [25, 26, 35] for the demonstration methodology. Note that in the EDG framework, the terms a_{Ps} vanish.

3.2. Implementation

In this section the final form of the discontinuous Galerkin formulation (65) is implemented within a conventional finite element framework. For the second–gradient problem, the interpolation polynomial order k is at least 2, with the

[1] The stability of the method can be demonstrated as in e.g. [25, 26, 35]. The minimum values of the stabilization parameters β^P and β^Q do not depend on the mesh size nor on the material properties, but solely on the element polynomial approximation considered. Practically considering values larger than 10 for quadratic elements will give similar results whatever their values, as it will be shown in the numerical examples.

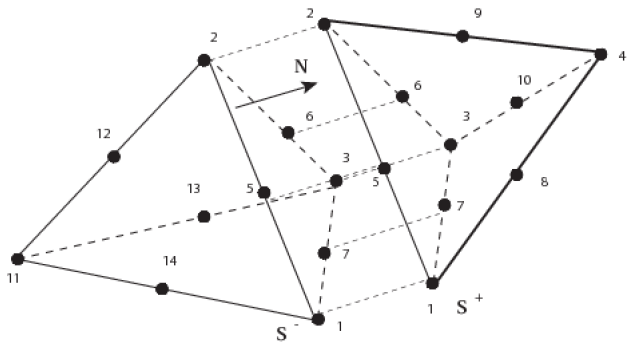

Figure 3: Interface element between two adjacent tetrahedra.

associated shape functions $N^a(\boldsymbol{\xi})$. The displacement field $\bar{\boldsymbol{u}}^h$ within the element is expressed in terms of the element nodal displacements $\bar{\boldsymbol{u}}^a$

$$\bar{u}_i^h(\boldsymbol{\xi}) = N^a(\boldsymbol{\xi})\,\bar{u}_i^a \text{ and } \delta\bar{u}_i = N^a(\boldsymbol{\xi})\,\delta\bar{u}_i^a\,. \tag{72}$$

Within the element the computations of the deformation gradient $\bar{\boldsymbol{F}}$ and of the gradient of deformation gradient $\bar{\boldsymbol{G}}$ require the first and second derivatives of the shape functions

$$\bar{F}_{ij} = \delta_{ij} + \frac{\partial\bar{u}_i^h}{\partial\bar{X}_j} = \delta_{ij} + \frac{\partial N^a(\boldsymbol{\xi})}{\partial\bar{X}_j}\bar{u}_i^a\,, \tag{73}$$

$$\delta\bar{F}_{ij} = \frac{\partial\delta\bar{u}_i}{\partial\bar{X}_j} = \frac{\partial N^a(\boldsymbol{\xi})}{\partial\bar{X}_j}\delta\bar{u}_i\,, \tag{74}$$

$$\bar{G}_{ijk} = \frac{\partial^2\bar{u}_i^h}{\partial\bar{X}_j\partial\bar{X}_k} = \frac{\partial^2 N^a(\boldsymbol{\xi})}{\partial\bar{X}_j\partial\bar{X}_k}\bar{u}_i^a\,, \text{ and} \tag{75}$$

$$\delta\bar{G}_{ijk} = \frac{\partial^2\delta\bar{u}_i}{\partial\bar{X}_j\partial\bar{X}_k} = \frac{\partial^2 N^a(\boldsymbol{\xi})}{\partial\bar{X}_j\partial\bar{X}_k}\delta\bar{u}_i^a\,. \tag{76}$$

The details of the calculations of the gradient of the shape function $\boldsymbol{\nabla}_0 N^a$ and of the second derivative $\boldsymbol{\nabla}_0 \otimes \boldsymbol{\nabla}_0 N^a$ are presented in Appendix A.

At each inter–element boundary, the surface element is inserted by splitting the degrees of freedom at the nodes common to the two adjacent elements (see Fig. 3). This new interface element is determined by the degrees of freedom of the two adjacent elements Ω_0^{e+} and Ω_0^{e-}. The jumps of the displacement and of its gradient are computed using the standard shape function interpolation

$$\left[\!\left[\bar{u}_i^h\right]\!\right] = N^a(\boldsymbol{\xi})\,(\bar{u}_i^{a+} - \bar{u}_i^{a-})\,, \qquad [\![\delta\bar{u}_i]\!] = N^a(\boldsymbol{\xi})\,(\delta\bar{u}_i^{a+} - \delta\bar{u}_i^{a-})\,, \tag{77}$$

$$\left[\!\left[\frac{\partial\bar{u}_i^h}{\partial\bar{X}_j}\right]\!\right] = \frac{\partial N^a(\boldsymbol{\xi})}{\partial\bar{X}_j}\,(\bar{u}_i^{a+} - \bar{u}_i^{a-})\,, \quad \text{and} \quad \left[\!\left[\frac{\partial\delta\bar{u}_i}{\partial\bar{X}_j}\right]\!\right] = \frac{\partial N^a(\boldsymbol{\xi})}{\partial\bar{X}_j}\,(\delta\bar{u}_i^{a+} - \delta\bar{u}_i^{a-})\,. \tag{78}$$

When using the EDG formulation, the jump of the displacement gradient is similar, but there is no jump on the displacement,

$$\left[\!\left[\bar{u}_i^h\right]\!\right] = 0\,, \text{ and } [\![\delta\bar{u}_i]\!] = 0\,, \tag{79}$$

and all the surface integrals a_{Ps} related to the displacement jumps vanish.

In the general FDG case, the mean effective stress $\hat{\boldsymbol{P}}$ is estimated from Eq. (49)

$$\begin{aligned}\hat{P}_{ij}^{\pm}\left(\bar{\boldsymbol{u}}^{h}\right) &= \bar{P}_{ij}^{\pm}\left(\bar{\boldsymbol{u}}^{h}\right) - \frac{\partial \bar{Q}_{ijk}^{\pm}\left(\bar{\boldsymbol{u}}^{h}\right)}{\partial \bar{X}_{k}} \\ &= \bar{P}_{ij}^{\pm}\left(\bar{\boldsymbol{u}}^{h}\right) - \mathcal{L}_{ijkpq}^{\bar{G}\bar{F}\pm}\left(\bar{\boldsymbol{u}}^{h}\right)\bar{G}_{kpq}^{\pm}\left(\bar{\boldsymbol{u}}^{h}\right) - \mathcal{J}_{ijkpqr}^{\pm}\left(\bar{\boldsymbol{u}}^{h}\right)\bar{K}_{pqrk}^{\pm}\left(\bar{\boldsymbol{u}}^{h}\right), \end{aligned} \tag{80}$$

where the third-order deformation gradient $\bar{K}_{pqrk}\left(\bar{\boldsymbol{u}}^{h}\right)$ is given by

$$\bar{K}_{pqrk}^{\pm}\left(\bar{\boldsymbol{u}}^{h}\right) = \frac{\partial^{3} N^{a}\left(\boldsymbol{\xi}\right)}{\partial \bar{X}_{q}\partial \bar{X}_{r}\partial \bar{X}_{k}}\bar{u}_{i}^{a\pm}, \tag{81}$$

and where the expression of the third gradient of the shape function is detailed in Appendix A.

The outer surface normal $\bar{\boldsymbol{N}}^{-}$ corresponding to the element Ω_{0}^{e-} is given by

$$\bar{\boldsymbol{N}}^{-} = \frac{\boldsymbol{G}^{1}\left(\boldsymbol{\xi}\right) \wedge \boldsymbol{G}^{2}\left(\boldsymbol{\xi}\right)}{\left\|\boldsymbol{G}^{1}\left(\boldsymbol{\xi}\right) \wedge \boldsymbol{G}^{2}\left(\boldsymbol{\xi}\right)\right\|}, \tag{82}$$

in which $G_{i}^{\alpha}\left(\boldsymbol{\xi}\right) = \frac{\partial N^{a}(\boldsymbol{\xi})}{\partial \bar{X}_{\alpha}}\bar{X}_{i}^{a}$ are the covariant base vectors with $\alpha = [1, 2]$.

Using the interpolations (72) to (78) in Eqs. (66) and (68), the weak form (65) can be rewritten as

$$\boldsymbol{f}^{\text{int}} + \boldsymbol{f}^{\text{s}} = \boldsymbol{f}^{\text{ext}}, \tag{83}$$

where $\boldsymbol{f}^{\text{int}}$ is the internal force vector computed from the volume integrals, $\boldsymbol{f}^{\text{s}}$ is the internal force vector computed from the surface integrals and $\boldsymbol{f}^{\text{ext}}$ is the external force vector. The volume integrals $a_{\text{PF}}^{e}\left(\bar{\boldsymbol{u}}^{h}, \delta\bar{\boldsymbol{u}}\right)$ and $a_{\text{QG}}^{e}\left(\bar{\boldsymbol{u}}^{h}, \delta\bar{\boldsymbol{u}}\right)$ are computed using Eqs. (73) to (76) and with a classical Gauss integration (4 Gauss points for quadratic tetrahedra and 27 Gauss points for quadratic hexahedra). The surface integrals are evaluated from Eqs. (80) to (82) by using the surface full quadrature rule (6 Gauss points for quadratic triangles as interface elements and 9 Gauss points for quadratic quadrangles as interface elements). For both volume and surface Gauss points, what remains to be defined are the stress tensor $\bar{\boldsymbol{P}}$ and the higher–order stress $\bar{\boldsymbol{Q}}$, both from $\bar{\boldsymbol{F}}$ and $\bar{\boldsymbol{G}}$. Toward this end, the micro–problems associated to each Gauss point have to be solved. The nonlinear equation (83) can be solved iteratively using a Newton–Raphson procedure. The consistent tangent stiffness matrix is assembled by taking into account the contributions from both volume and surface parts and is provided in Appendix B.

This framework has been implemented in the parallel code Gmsh [38]. The implementation is based on the partitioning of the mesh at the macro–scale. The connectivity between partitions is ensured using the face–based ghost method for discontinuous Galerkin method described in [35, 36]. The elements of the macro–mesh are thus integrated in different processors. During this integration the Gauss points of a bulk or interface element call a constitutive material law, which consists into the resolution of a micro–scale problem if the computational homogenization is considered. The repartition of the micro–scale problems resolution is thus naturally divided among the processors.

3.3. Numerical validation

To validate the discontinuous Galerkin formulation presented above, the 3–dimensional shear layer test shown in Fig. 4 is studied. The layer has a height H in the Y-direction and an infinite length in the two other directions X and Z, and thus all quantities depend only on the position Y. Although the problem is strictly 1–dimensional, 3–dimensional meshes are used in order to validate the 3–dimensional implementation of the discontinuous Galerkin method. A 3–dimensional shear strip is extracted from the layer. The two displacement components in the Y and Z directions are fixed, while the periodic boundary condition is applied between the left and right surfaces of the strip mesh in the X direction.

The theoretical solution of this shear layer can be obtained in a closed form for an elastic strain gradient solid characterized by the shear modulus μ, which relates the shear stress σ_{xy} to the shear strain $\frac{\partial u}{\partial y}$, and by the higher–order

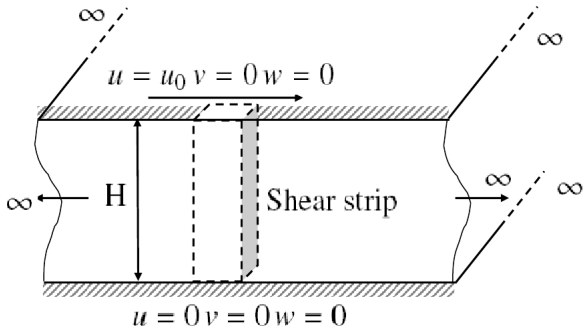

Figure 4: The 3–dimensional shear layer problem and the extracted shear strip.

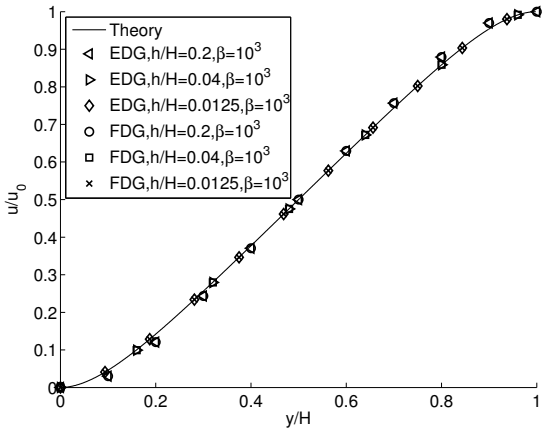

Figure 5: Displacement field obtained using the EDG and FDG methods for different mesh sizes is compared to the theoretical solution of the shear layer problem –layer height $H = 1$mm, internal length scale parameter $l = 0.1$mm, stabilization parameters $\beta^P = \beta^Q = \beta = 1000$.

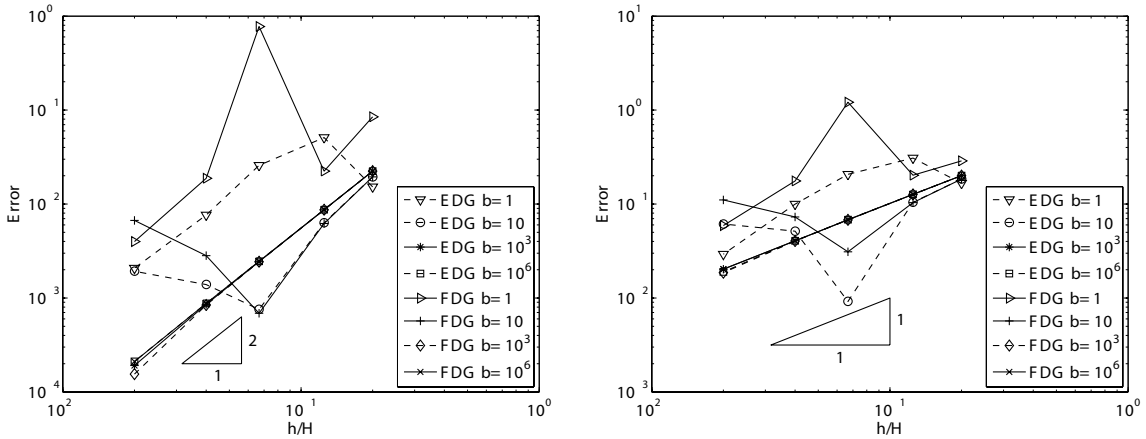

(a) $\boldsymbol{L}^2$–norm (b) $\boldsymbol{H}^1$–norm

Figure 6: Error with respect to the mesh size of the shear layer problem with the EDG and FDG methods and for different stabilization parameters $\beta^P = \beta^Q = \beta$ –layer height $H = 1$mm, internal length scale parameter $l = 0.1$mm. (a) Error in the $\boldsymbol{L}^2$–norm and (b) Error in the $\boldsymbol{H}^1$–norm.

modulus κ, which relates the higher–order stress τ_{xyy} to the higher–order displacement gradient $\frac{\partial^2 u}{\partial y^2}$, such as

$$\sigma_{xy} = \mu \frac{\partial u}{\partial y} \text{ and } \tau_{xyy} = \kappa \frac{\partial^2 u}{\partial y^2} \,. \tag{84}$$

The governing equation (12) can be approximated in the small strain case by

$$\frac{\partial}{\partial y}\left[\mu \frac{\partial u}{\partial y} - \frac{\partial}{\partial y}\left(\kappa \frac{\partial u}{\partial y^2}\right)\right] = 0 \,, \tag{85}$$

with the boundary conditions at the extremities

$$u(y=0) = 0 \,,\, \frac{\partial u}{\partial y}(y=0) = 0 \text{ and} \tag{86}$$

$$u(y=H) = u_0 \,,\, \frac{\partial u}{\partial y}(y=H) = 0 \,. \tag{87}$$

By using the definition of the internal characteristic length parameter $l = \sqrt{\frac{\kappa}{\mu}}$, the analytical solution of the ordinary equation (85) is

$$\frac{u\,(y)}{u_0} = \frac{\tanh\left(\frac{H}{l}\right)}{2 - \frac{H}{l}\tanh\left(\frac{H}{l}\right)}\left[\sinh\left(\frac{y}{l}\right) - \frac{y}{l}\right] + \frac{1 - \cosh\left(\frac{H}{l}\right)}{\cosh\left(\frac{H}{l}\right)\left[2 - \frac{H}{l}\tanh\left(\frac{H}{l}\right)\right]}\left[\cosh\left(\frac{y}{l}\right) - 1\right] \,. \tag{88}$$

Clearly the solution depends on the ratio $\frac{H}{l}$ introducing a size effect in the shear layer problem.

The solution of this shear layer problem is numerically studied using the presented FDG and the EDG methods for a layer height $H = 1$mm and an internal characteristic length $l = 0.1$mm. In order to assess the convergence of this method with respect to the mesh size h, simulations are conducted for a series of mesh sizes, with different stabilization parameters $\beta^P = \beta^Q = \beta$, and with quadratic brick elements. Fig. 5 illustrates the displacement obtained for the different the mesh size with $\beta = 1000$. The solution fully converges to the theoretical result. The convergence with respect to the mesh size in the $\boldsymbol{L}^2$–norm and in the $\boldsymbol{H}^1$–norm (71) obtained for different stabilization parameters are respectively shown in Fig. 6a and Fig. 6b. The convergence rate in the $\boldsymbol{L}^2$–norm and in $\boldsymbol{H}^1$–norm are respectively equal to 2 and 1 when $\beta^P = \beta^Q > 10$, which are the theoretical values when using quadratic element. This confirms that the method is stable for the values of β larger than a constant. As the time requires to solve the macro–problem becomes negligible compared to the resolution of the micro–problems, the use of the FDG method is more advantageous since the method is amenable to an efficient parallel implementations using a face–based ghost method [35, 36].

4. Solution at the microscopic scale

The microscopic boundary value problem presented in section 2.2 is a standard quasi–static nonlinear problem. From the definition of the fluctuation field (20), the periodic constraints (24) and (27) can be rewritten in the matrix form by switching from tensorial notations to vector notations in the finite element discretization, yielding

$$\boldsymbol{C}\boldsymbol{u} = \boldsymbol{g} \,, \tag{89}$$

where $\boldsymbol{u}$ is the finite displacement vector, where $\boldsymbol{g} = \boldsymbol{S}\left(\bar{\boldsymbol{F}} - \boldsymbol{I}\right) + \boldsymbol{T}\bar{\boldsymbol{G}}$ is the right hand side of the periodic constraint and where $\boldsymbol{S}$ and $\boldsymbol{T}$ are respectively the first and second kinematic matrix, which only depend on the boundary coordinates. The solution can be expressed by the minimization of the internal energy W^m_{int}

$$\min_{\boldsymbol{u}} W^m_{\text{int}} = \int_{V_0} \mathrm{U}^m \, dV \,, \qquad \text{subject to} \quad \boldsymbol{C}\boldsymbol{u} = \boldsymbol{g} \,, \tag{90}$$

where $\mathrm{U}^m = \mathrm{U}^m\left(\boldsymbol{F}^T\boldsymbol{F}\right)$ is the internal energy density. The Lagrange function is defined from the minimization problem

$$\Pi^m\left(\boldsymbol{u},\boldsymbol{\lambda},\bar{\boldsymbol{F}},\bar{\boldsymbol{G}}\right) = W^m_{\text{int}}(\boldsymbol{u}) - \boldsymbol{\lambda}^T\left[\boldsymbol{C}\boldsymbol{u} - \boldsymbol{g}\left(\bar{\boldsymbol{F}},\bar{\boldsymbol{G}}\right)\right], \tag{91}$$

where $\boldsymbol{\lambda}^T$ is the Lagrange multipliers vector. The stationary point of the Lagrange function (91) corresponds to the microscopic equilibrium state

$$\begin{aligned} \boldsymbol{f} - \boldsymbol{C}^T\boldsymbol{\lambda} &= \boldsymbol{0}, \\ \boldsymbol{C}\boldsymbol{u} - \boldsymbol{g} &= \boldsymbol{0}, \end{aligned} \tag{92}$$

where $\boldsymbol{f} = \frac{\partial W^m_{\text{int}}}{\partial \boldsymbol{u}}$ is the internal nodal force vector. There exist many methods to solve Eqs. (92). One is the Lagrange multipliers method, which considers the new degrees of freedom vector $\tilde{\boldsymbol{u}}^T = \left[\boldsymbol{u}^T \quad \boldsymbol{\lambda}^T\right]$ [4], but this approach increases the number of unknowns. Another method is to eliminate the constraints from the system by replacing all dependent degrees of freedom by the independent degrees of freedom [7, 9]. This approach reduces the system size but depends on the nature of the boundary conditions (the form of the matrix $\boldsymbol{C}$). In [4, 7, 9], the periodic boundary condition is only applied in case of conforming meshes –two opposite sides of the RVE have the same mesh distribution. On arbitrary meshes another method, as the polynomial interpolation method [37], must be used to constrain the boundary conditions. In that case the matrix $\boldsymbol{C}$ has an arbitrary form.

For the unified enforcement of these constraints, the multiple–constraint projection method [39, 8] is adopted in this paper and is described here below. Afterward, the extraction of the macros-scale material law is detailed.

4.1. Linear constraint enforcement

By using the multiple–constraint projection method, the number of unknowns is not modified. During the Newton–Raphson procedure, the linearized equations of the system (92) read

$$\boldsymbol{r} + \boldsymbol{K}\delta\boldsymbol{u} - \boldsymbol{C}\delta\boldsymbol{\lambda} = \boldsymbol{0}, \quad \text{and} \tag{93}$$

$$\boldsymbol{r}_c + \boldsymbol{C}\delta\boldsymbol{u} = \boldsymbol{0}, \tag{94}$$

where $\boldsymbol{r} = \boldsymbol{f} - \boldsymbol{C}^T\boldsymbol{\lambda}$ is the force residual vector, where $\boldsymbol{r}_c = \boldsymbol{C}\boldsymbol{u} - \boldsymbol{g}$ is the constraint residual vector, and where $\boldsymbol{K} = \frac{\partial \boldsymbol{f}}{\partial \boldsymbol{u}}$ is the stiffness matrix.

Because of the linear independence of all constraints in Eq. (89) the matrix $\boldsymbol{R} = \boldsymbol{C}^T\left(\boldsymbol{C}\boldsymbol{C}^T\right)^{-1}$ exists, which is not always the case of the matrix $\left(\boldsymbol{C}^T\boldsymbol{C}\right)^{-1}$. The matrix $\boldsymbol{R}$ should thus be introduced during the elimination of the Lagrange multipliers in order to solve the system of Eqs. (93-94). Using Eq. (93) leads to

$$\delta\boldsymbol{\lambda} = \boldsymbol{R}^T\left(\boldsymbol{r} + \boldsymbol{K}\delta\boldsymbol{u}\right), \tag{95}$$

which yields

$$\boldsymbol{Q}^T\left(\boldsymbol{r} + \boldsymbol{K}\delta\boldsymbol{u}\right) = \boldsymbol{0}, \tag{96}$$

where the matrix $\boldsymbol{Q} = \boldsymbol{I} - \boldsymbol{R}\boldsymbol{C}$. From this definition one has $\boldsymbol{Q}\delta\boldsymbol{u} = \delta\boldsymbol{u} - \boldsymbol{R}\boldsymbol{C}\delta\boldsymbol{u}$ and Eqs. (94) can be rewritten

$$\delta\boldsymbol{u} = \boldsymbol{Q}\delta\boldsymbol{u} - \boldsymbol{R}\boldsymbol{r}_c. \tag{97}$$

On the one hand, combining Eqs. (96) and (97) leads to

$$\boldsymbol{Q}^T\boldsymbol{K}\boldsymbol{Q}\delta\boldsymbol{u} + \boldsymbol{Q}^T\left(\boldsymbol{r} - \boldsymbol{K}\boldsymbol{R}\boldsymbol{r}_c\right) = \boldsymbol{0}, \tag{98}$$

and on the other hand, the constraint (94) can be rewritten as

$$\boldsymbol{C}^T\boldsymbol{r}_c + \boldsymbol{C}^T\boldsymbol{C}\delta\boldsymbol{u} = \boldsymbol{0}. \tag{99}$$

The sum of these last two Eqs. (98) and (99) eventually leads to

$$\left(\boldsymbol{C}^T\boldsymbol{C} + \boldsymbol{Q}^T\boldsymbol{K}\boldsymbol{Q}\right)\delta\boldsymbol{u} + \boldsymbol{C}^T\boldsymbol{r}_c + \boldsymbol{Q}^T\left(\boldsymbol{r} - \boldsymbol{K}\boldsymbol{R}\boldsymbol{r}_c\right) = \boldsymbol{0}\,, \tag{100}$$

which can be written under the form

$$\delta\boldsymbol{u} = -\tilde{\boldsymbol{K}}^{-1}\tilde{\boldsymbol{r}}\,, \tag{101}$$

where

$$\tilde{\boldsymbol{K}} = \boldsymbol{C}^T\boldsymbol{C} + \boldsymbol{Q}^T\boldsymbol{K}\boldsymbol{Q}\,, \quad \text{and} \tag{102}$$

$$\tilde{\boldsymbol{r}} = \boldsymbol{C}^T\boldsymbol{r}_c + \boldsymbol{Q}^T\left(\boldsymbol{r} - \boldsymbol{K}\boldsymbol{R}\boldsymbol{r}_c\right)\,. \tag{103}$$

As proved in [39], the solution (101) is the unique solution of the system of equations (93-94).

4.2. Macroscopic first Piola–Kirchhoff stress and macroscopic higher–order stress tensors

The macroscopic stresses can be obtained from Eq. (91) following

$$\bar{\boldsymbol{P}} = \frac{1}{V_0}\frac{\partial\Pi^m}{\partial\bar{\boldsymbol{F}}} = \frac{1}{V_0}\boldsymbol{S}^T\boldsymbol{\lambda}\,, \quad \text{and} \tag{104}$$

$$\bar{\boldsymbol{Q}} = \frac{1}{V_0}\frac{\partial\Pi^m}{\partial\bar{\boldsymbol{G}}} = \frac{1}{V_0}\boldsymbol{T}^T\boldsymbol{\lambda}\,. \tag{105}$$

Practically, the macroscopic stresses are computed from Eqs. (104) and (105) by using the Lagrange multipliers $\boldsymbol{\lambda}$, which are given at the equilibrium state $\boldsymbol{r} = \boldsymbol{0}$ by

$$\boldsymbol{\lambda} = \boldsymbol{R}^T\boldsymbol{f}\,. \tag{106}$$

The first Piola–Kirchhoff stress and the higher–order stress tensors are thus obtained from

$$\bar{\boldsymbol{P}} = \frac{1}{V_0}\boldsymbol{S}^T\boldsymbol{R}^T\boldsymbol{f}\,, \quad \text{and} \tag{107}$$

$$\bar{\boldsymbol{Q}} = \frac{1}{V_0}\boldsymbol{T}^T\boldsymbol{R}^T\boldsymbol{f}\,. \tag{108}$$

4.3. Macroscopic constitutive tangent operators

To estimate the tangent operators, the static condensation procedure developed in [7] is considered. Note that the supplementary constraints (27) act as fixations on the mean values of the boundary displacement field and that no extra explicit fixations are required to prevent the rigid body motion. In this paper the static condensation idea is extended to the use of Lagrange multipliers. Toward this end, the linearization around the equilibrium state of the micro–scale system (93) is rearranged as

$$\begin{bmatrix}\boldsymbol{K}_{ii} & \boldsymbol{K}_{ib}\\ \boldsymbol{K}_{bi} & \boldsymbol{K}_{bb}\end{bmatrix}\begin{bmatrix}\delta\boldsymbol{u}_i\\ \delta\boldsymbol{u}_b\end{bmatrix} = \begin{bmatrix}\boldsymbol{0}\\ \boldsymbol{C}^T\delta\boldsymbol{\lambda}\end{bmatrix}\,, \tag{109}$$

where $\boldsymbol{u}_i$ and $\boldsymbol{u}_b$ are respectively the internal and the boundary nodal displacement vectors and where $\boldsymbol{K}_{ii}, \boldsymbol{K}_{ib}, \boldsymbol{K}_{bi}$ and $\boldsymbol{K}_{bb}$ are the four related parts of the stiffness matrix $\boldsymbol{K}$. Eq. (109) is equivalent to the system

$$\tilde{\boldsymbol{K}}_{bb}\delta\boldsymbol{u}_b = \boldsymbol{C}^T\delta\boldsymbol{\lambda} \text{ with } \tilde{\boldsymbol{K}}_{bb} = \boldsymbol{K}_{bb} - \boldsymbol{K}_{bi}\boldsymbol{K}_{ii}^{-1}\boldsymbol{K}_{ib}\,. \tag{110}$$

Note that the matrix $\tilde{\boldsymbol{K}}_{bb}$ is usually singular. For expressing $\delta\boldsymbol{\lambda}$ in terms of the macroscopic quantities, the linear constraints (89) are now rewritten in terms of the boundary degrees of freedom only

$$\boldsymbol{C}_b\delta\boldsymbol{u}_b = \boldsymbol{S}\delta\bar{\boldsymbol{F}} + \boldsymbol{T}\delta\bar{\boldsymbol{G}}\,. \tag{111}$$

Because of the linear independence of the linear constraints created from the periodic boundary condition, the boundary degrees of freedom can always be decomposed into a dependent part $\boldsymbol{u}_{bd}$ and into an independent part $\boldsymbol{u}_{bi}$ as

$$\boldsymbol{C}_b \delta\boldsymbol{u}_b = \boldsymbol{C}_{bd} \delta\boldsymbol{u}_{bd} + \boldsymbol{C}_{bi} \delta\boldsymbol{u}_{bi} \,, \tag{112}$$

where the size of the dependent part $\boldsymbol{u}_{bd}$ is equal to the number of constraints from the boundary condition. The selection of this part is arbitrary as long as the matrix $\boldsymbol{C}_{bd}$ is invertible. For periodic meshes, the dependent and independent parts are respectively the degrees of freedom on the positive part and on the negative part of the RVE boundary. For arbitrary meshes and when using the polynomial interpolation method, the independent part corresponds to the new degrees of freedom introduced in the problem to define the polynomial approximation of the boundary, while the dependent part corresponds to the original degrees of freedom of the RVE boundary, see [37].

From (111) and (112) the new linear constraints are given by

$$\delta\boldsymbol{u}_{bd} = \boldsymbol{C}_{di} \delta\boldsymbol{u}_{bi} + \boldsymbol{S}_{di} \delta\bar{\boldsymbol{F}} + \boldsymbol{T}_{di} \delta\bar{\boldsymbol{G}} \tag{113}$$

where $\boldsymbol{C}_{di} = -\boldsymbol{C}_{bd}^{-1}\boldsymbol{C}_{bi}$, $\boldsymbol{S}_{di} = \boldsymbol{C}_{bd}^{-1}\boldsymbol{S}$ and where $\boldsymbol{T}_{di} = \boldsymbol{C}_{bd}^{-1}\boldsymbol{T}$. Because of the decomposition of the boundary degrees of freedom (112), the force equilibrium (110) can be rewritten as

$$\begin{bmatrix} \tilde{\boldsymbol{K}}_{dd} & \tilde{\boldsymbol{K}}_{di} \\ \tilde{\boldsymbol{K}}_{id} & \tilde{\boldsymbol{K}}_{ii} \end{bmatrix} \begin{bmatrix} \delta\boldsymbol{u}_{bd} \\ \delta\boldsymbol{u}_{bi} \end{bmatrix} = \begin{bmatrix} \boldsymbol{C}_{bd}^T \delta\boldsymbol{\lambda} \\ \boldsymbol{C}_{bi}^T \delta\boldsymbol{\lambda} \end{bmatrix} , \tag{114}$$

where $\tilde{\boldsymbol{K}}_{dd}, \tilde{\boldsymbol{K}}_{di}, \tilde{\boldsymbol{K}}_{id}$ and $\tilde{\boldsymbol{K}}_{ii}$ are the four related parts of the stiffness $\tilde{\boldsymbol{K}}_{bb}$. Using Eqs.(113) and (114) leads to the expression of the Lagrange multipliers in terms of the macroscopic quantities

$$\delta\boldsymbol{\lambda} = \boldsymbol{C}_{bd}^{-T} \boldsymbol{K}_{dd}^{*} \left(\boldsymbol{S}_{di} \delta\bar{\boldsymbol{F}} + \boldsymbol{T}_{di} \delta\bar{\boldsymbol{G}} \right) , \tag{115}$$

where $\boldsymbol{K}_{dd}^{*} = \tilde{\boldsymbol{K}}_{dd} - \boldsymbol{K}_{id}^{*T} \boldsymbol{K}_{ii}^{*-1} \boldsymbol{K}_{id}^{*}$, $\boldsymbol{K}_{id}^{*} = \tilde{\boldsymbol{K}}_{id} + \boldsymbol{C}_{di}^T \tilde{\boldsymbol{K}}_{dd}$ and $\boldsymbol{K}_{ii}^{*} = \tilde{\boldsymbol{K}}_{ii} + \boldsymbol{C}_{di}^T \tilde{\boldsymbol{K}}_{di} + \tilde{\boldsymbol{K}}_{id} \boldsymbol{C}_{di} + \boldsymbol{C}_{di}^T \tilde{\boldsymbol{K}}_{dd} \boldsymbol{C}_{di}$. Eventually, combining Eqs. (104), (105), and (115) gives

$$\delta\bar{\boldsymbol{P}} = \frac{1}{V_0} \boldsymbol{S}_{di}^T \boldsymbol{K}_{dd}^{*} \left(\boldsymbol{S}_{di} \delta\bar{\boldsymbol{F}} + \boldsymbol{T}_{di} \delta\bar{\boldsymbol{G}} \right) , \text{ and} \tag{116}$$

$$\delta\bar{\boldsymbol{Q}} = \frac{1}{V_0} \boldsymbol{T}_{di}^T \boldsymbol{K}_{dd}^{*} \left(\boldsymbol{S}_{di} \delta\bar{\boldsymbol{F}} + \boldsymbol{T}_{di} \delta\bar{\boldsymbol{G}} \right) . \tag{117}$$

Since in the second–order computational homogenization framework the macro–structure is modeled as a full second gradient continuum, the linearized constitutive relations can always be written in the form

$$\delta\bar{\boldsymbol{P}} = \boldsymbol{C} : \delta\bar{\boldsymbol{F}} + \boldsymbol{\mathcal{L}}^{\bar{F}\bar{G}} \vdots \delta\bar{\boldsymbol{G}} , \text{ and} \tag{118}$$

$$\delta\bar{\boldsymbol{Q}} = \boldsymbol{\mathcal{L}}^{\bar{G}\bar{F}} : \delta\bar{\boldsymbol{F}} + \boldsymbol{\mathcal{J}} \vdots \delta\bar{\boldsymbol{G}} . \tag{119}$$

Comparing these last equations with Eqs. (116) and (117), the tangent operators are given in the matrix notations by

$$\boldsymbol{C} = \frac{1}{V_0} \boldsymbol{S}_{di}^T \boldsymbol{K}_{dd}^{*} \boldsymbol{S}_{di} \,, \tag{120}$$

$$\boldsymbol{\mathcal{L}}^{\bar{F}\bar{G}} = \frac{1}{V_0} \boldsymbol{S}_{di}^T \boldsymbol{K}_{dd}^{*} \boldsymbol{T}_{di} \,, \tag{121}$$

$$\boldsymbol{\mathcal{L}}^{\bar{G}\bar{F}} = \frac{1}{V_0} \boldsymbol{T}_{di}^T \boldsymbol{K}_{dd}^{*} \boldsymbol{S}_{di} \,, \text{ and} \tag{122}$$

$$\boldsymbol{\mathcal{J}} = \frac{1}{V_0} \boldsymbol{T}_{di}^T \boldsymbol{K}_{dd}^{*} \boldsymbol{T}_{di} \,. \tag{123}$$

Finally, the constitutive tangent operators are directly obtained by the static condensation of the microscopic global

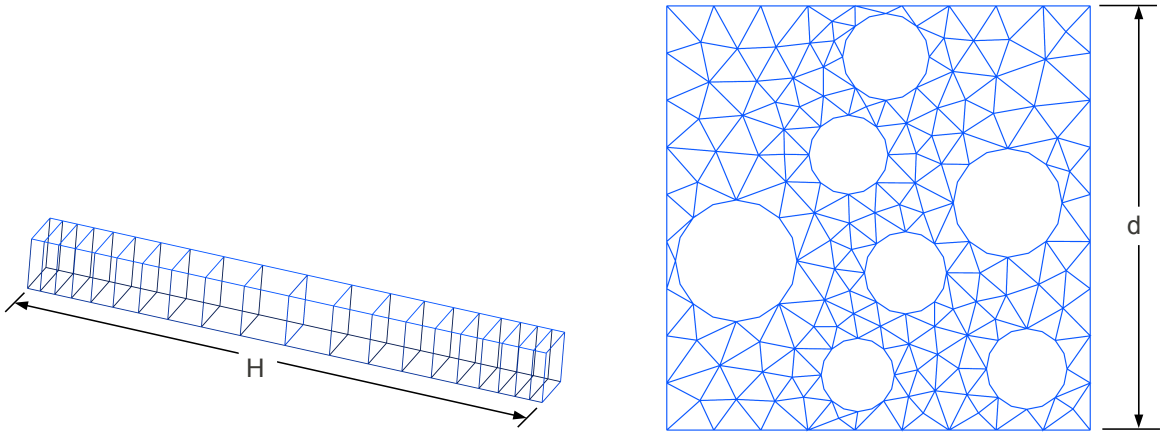

(a) Macroscopic mesh (b) Microscopic mesh

Figure 7: (a) The shear strip mesh and (b) the RVE mesh for the multiscale computational homogenization analysis of the shear layer problem. The width of the shear layer is H and the size of RVE is d. The effect of the ratio $\frac{H}{d}$ on the results illustrates the size effect.

stiffness matrix with the linear constraint matrix. In the non–linear case, the tangent operator estimation automatically includes the geometrical and material non–linearity contributions. For the linear case, this scheme leads to a direct quantification of the macroscopic elastic stiffness (e.g. of Mindlin model) based on the micro–analysis.

5. Numerical example: the shear layer problem

In this section, the boundary layer problem (see Fig. 4) is reconsidered by using the second–order multiscale computational homogenization approach. This test is often used in literature as a benchmark problem for higher–order continuum analyzes, e.g. in [7, 8, 24, 23, 40]. At the macroscopic scale, the shear layer height H varies between 1mm and 8mm. The mesh of the shear strip is shown in Fig. 7a. At the microscopic scale, because of the plane strain state, a 2–dimensional RVE is considered with randomly distributed holes of 26% void fraction as shown in Fig. 7b. The size of this RVE is taken to be $d = 0.2$mm and is kept unchanged during the study. By varying the macroscopic size H, while keeping the microscopic RVE size unchanged, the influence of the ratio $\frac{H}{d}$ on the shear layer behavior can be investigated. An elasto–plastic material model is used as a microscopic material law. In this law, the deformation gradient $\boldsymbol{F}$ is decomposed into the reversible elastic part $\boldsymbol{F}^e$ and into the irreversible plastic part $\boldsymbol{F}^p$ such that $\boldsymbol{F} = \boldsymbol{F}^e \cdot \boldsymbol{F}^p$. The elastic potential energy is defined by

$$\mathrm{U}^m(\boldsymbol{C}^e) = \frac{K_0}{2} \log^2 J + \frac{\mu_0}{4} (\log \boldsymbol{C}^e)^{\mathrm{dev}} : (\log \boldsymbol{C}^e)^{\mathrm{dev}} \,, \tag{124}$$

where $J = \det \boldsymbol{F}$ and where $\boldsymbol{C}^e = \boldsymbol{F}^{eT} \cdot \boldsymbol{F}^e$. The first Piola–Kirchhoff stress tensor is then calculated by the relation

$$\boldsymbol{P} = 2\boldsymbol{F} \cdot \left[(\boldsymbol{F}^p)^{-1} \cdot \frac{\partial \mathrm{U}^m(\boldsymbol{C}^e)}{\partial \boldsymbol{C}^e} \cdot (\boldsymbol{F}^p)^{-T} \right] . \tag{125}$$

The Cauchy stress can thus be deduced via $\boldsymbol{\sigma} = J^{-1} \boldsymbol{P} \cdot \boldsymbol{F}^T$ and the equivalent von Mises stress is evaluated via

$$\sigma_{VM} = \sqrt{\frac{3}{2} \mathrm{dev}\,(\boldsymbol{\sigma}) : \mathrm{dev}\,(\boldsymbol{\sigma})} \,, \tag{126}$$

which allows to estimate the yield function

$$f = \sigma_{VM} - \sigma_y(p) \leq 0 \,. \tag{127}$$

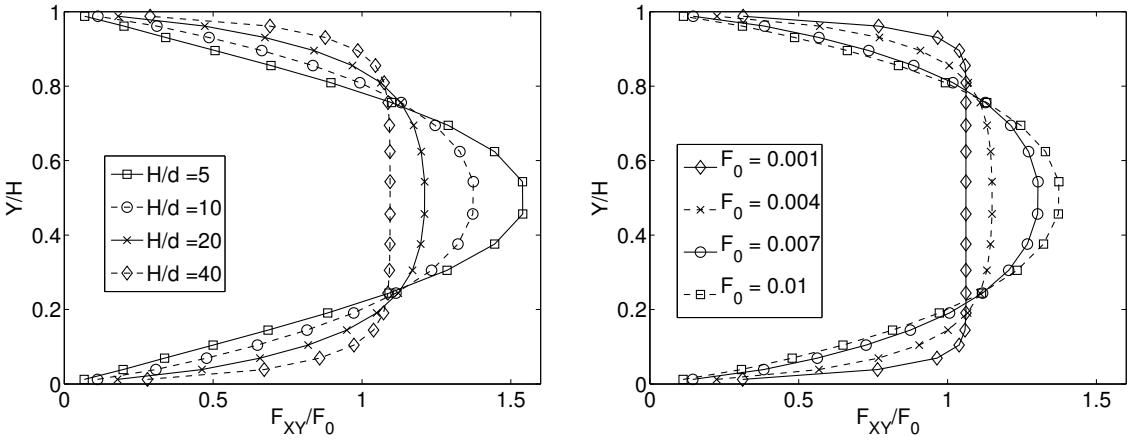

(a) Size effect at $F_0 = 0.01$ (b) Development of the boundary effect with $\frac{H}{d} = 10$

Figure 8: (a) The distribution of the shear strain F_{XY} across the shear layer for several values of $\frac{H}{d}$ and (b) the development of the boundary effect in the shear layer at various shear values F_0 and for $\frac{H}{d} = 10$. At the macroscopic scale, the FDG method is used with the stabilization parameters $\beta^P = \beta^Q = 1000$.

In this last equation, p is the equivalent plastic strain and $\sigma_y(p)$ is the yield stress, which is defined by the hardening law. In case of a linear hardening law, $\sigma_y(p)$ is given by the relation

$$\sigma_y(p) = \sigma_y^0 + hp\,, \tag{128}$$

where σ_y^0 is the initial yield stress and where h is the hardening modulus. In this section, the material parameters correspond to a bulk modulus $K_0 = 175$GPa, a shear modulus $\mu_0 = 81$GPa, an initial yield stress $\sigma_Y^0 = 507$MPa, and a constant hardening modulus $h = 200$MPa. The macroscopic prescribed shear strain is $F_0 = 0.01$, which yields the macroscopic prescribed displacement $u_0 = F_0 H$. At the macroscopic scale, the FDG formulation is used with the stabilization parameters $\beta^P = \beta^Q = 1000$. The simulations have been run in parallel with one macro–element per processor.

Homogeneous results would be found across the layer with a classical multiscale computational scheme. On the contrary, the second–order multiscale computational homogenization incorporates the macroscopic response with the micro–structural size and accounts for the vanishing of shear strain at the layer extremities, which leads to a non–uniform response across the layer. Fig. 8a shows the distribution of shear strain F_{XY} across the layer at the prescribed shear strain $F_0 = 0.01$. The shear strain vanishes at the layer extremities and is maximum at the layer center. As it can be seen, the thickness of the zone with boundary effect increases when the ratio $\frac{H}{d}$ decreases. For the case $\frac{H}{d} = 5$, where the micro–structural size is comparable with the macroscopic size, the boundary effect fully covers along the height of the shear layer. The responses for different values of the ratio $\frac{H}{d}$ are clearly separated.

Fig. 8b shows the development of the boundary effect across the layer at different prescribed shear strains F_0 for $\frac{H}{d} = 10$. The thickness of the zone with the boundary effects depends not only on the ratio $\frac{H}{d}$ as shown in Fig. 8a, but also on the value of the prescribed macroscopic shear strain F_0 as shown in Fig. 8b. The larger the prescribed macroscopic shear strain, the more important the plasticity. Moreover, it can be seen that the boundary effect depends on the plastic behavior.

Fig. 9 shows the deformed macroscopic mesh and the distribution of the equivalent plastic strain in several RVEs associated to the shear layer for $\frac{H}{d} = 10$ and for $\frac{H}{d} = 40$. For $\frac{H}{d} = 10$, the shear profile is non–uniform and the distribution of the equivalent plastic strain is distinguishable from each RVE with a concentration at the layer center. On other hand, we can observe an almost constant distribution of the equivalent plastic strain in each RVE for $\frac{H}{d} = 40$.

This numerical example clearly demonstrates the ability of the discontinuous Galerkin method for solving the second–order continua, not only in macroscopic continuum, but also in the context of the second–order multiscale

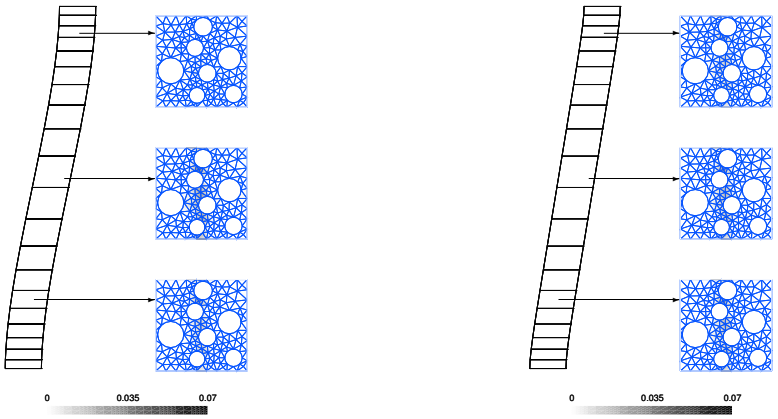

(a) Deformed macroscopic shape with $\frac{H}{d} = 10$ (b) Deformed macroscopic shape with $\frac{H}{d} = 40$

Figure 9: The deformation of the macroscopic mesh at $F_0 = 0.01$ –displacements are magnified 15 times– and the distribution of the equivalent plastic strain in several RVEs associated to the shear layer. The FDG method is used with the stabilization parameters $\beta^P = \beta^Q = 1000$.

computational homogenization.

6. Conclusions and perspectives

This paper proposes a new framework for the second–order multiscale computational homogenization procedure, which incorporates the second–order continuum at the macroscopic scale while considering the classical continuum at the microscopic scale. The macroscopic second–order continua is resolved by using the discontinuous Galerkin method for which the continuities of the displacement and of its derivatives are weakly enforced. The advantage of using discontinuous Galerkin techniques is to use only the displacement field as unknowns. The implementation of the presented framework shows that it can be integrated into conventional parallel finite element codes in a straightforward way.

The important feature of the second–order multiscale computational homogenization procedure is to incorporate a length scale via the size of the microscopic RVE. This allows moderate localization bands and size effects to be captured. This proposed homogenization procedure using the discontinuous Galerkin method will be used in the near future to model the localization and size effects in foamed materials.

Acknowledgment

Les recherches ont été financées grâce à la subvention “Actions de recherche concertées ARC 09/14-02 BRIDGING - From imaging to geometrical modelling of complex micro structured materials: Bridging computational engineering and material science” de la Direction générale de l’Enseignement non obligatoire de la Recherche scientifique, Direction de la Recherche scientifique, Communauté française de Belgique, et octroyées par l’Académie Universitaire Wallonie-Europe.

Appendix A. Derivatives of the shape functions

In the finite element method, the shape functions are used to approximate all the continuous fields within the finite element. In general, the shape function in the iso–parametric space reads

$$N = N(\boldsymbol{\xi}) \,. \tag{A.1}$$

In the element space, the shape function values and its derivatives can be calculated:

$$N(\boldsymbol{X})\,,\ \frac{\partial N}{\partial \boldsymbol{X}}\,,\ \frac{\partial^2 N}{\partial \boldsymbol{X}\partial \boldsymbol{X}} \text{ and } \frac{\partial^3 N}{\partial \boldsymbol{X}\partial \boldsymbol{X}\partial \boldsymbol{X}}\,. \tag{A.2}$$

The Jacobian matrix which transforms the iso–parametric space to the element space, is defined as

$$J_{ij} = \frac{\partial X_j}{\partial \xi_i} \text{ and } J^{-1}_{ij} = \frac{\partial \xi_j}{\partial X_i}\,. \tag{A.3}$$

All the derivatives of the shape function are computed easily in the iso–parametric space:

$$B^{\xi}_m = \frac{\partial N}{\partial \xi_m}\,,\quad H^{\xi}_{mn} = \frac{\partial^2 N}{\partial \xi_m \partial \xi_n} \text{ and } K^{\xi}_{mnp} = \frac{\partial^3 N}{\partial \xi_m \partial \xi_n \partial \xi_p}\,. \tag{A.4}$$

The values on the element space follow from:

Appendix A.1. Value of the shape function

$$N(\boldsymbol{X}) = N(\boldsymbol{\xi})\,. \tag{A.5}$$

Appendix A.2. First derivative of the shape function

$$B_j = \frac{\partial N}{\partial X_j} = \frac{\partial N}{\partial \xi_m}\frac{\partial \xi_m}{\partial X_j} = J^{-1}_{jm} B^{\xi}_m\,. \tag{A.6}$$

Appendix A.3. Second derivative of the shape function

$$H_{jk} = \frac{\partial^2 N}{\partial X_j \partial X_k} = \frac{\partial}{\partial X_k}\left(\frac{\partial N}{\partial \xi_m}\frac{\partial \xi_m}{\partial X_j}\right) = J^{-1}_{kr}\frac{\partial}{\partial \xi_r}\left(J^{-1}_{jm} B^{\xi}_m\right) = J^{-1}_{jm} J^{-1}_{kr} H^{\xi}_{mr} + J^{-1}_{kr} B^{\xi}_m \frac{\partial J^{-1}_{jm}}{\partial \xi_r}\,. \tag{A.7}$$

Let

$$\mathcal{A}_{jmr} = \frac{\partial J^{-1}_{jm}}{\partial \xi_r}\,, \tag{A.8}$$

be computed from

$$J^{-1}_{jp} J_{pm} = \delta_{jm} \tag{A.9}$$

$$\Leftrightarrow \qquad \frac{\partial J^{-1}_{jp}}{\partial \xi_r} J_{pm} + J^{-1}_{jp}\frac{\partial J_{pm}}{\partial \xi_r} = 0 \tag{A.10}$$

$$\Leftrightarrow \qquad \mathcal{A}_{jmr} = \frac{\partial J^{-1}_{jm}}{\partial \xi_r} = -J^{-1}_{jp}\frac{\partial J_{pq}}{\partial \xi_r} J^{-1}_{qm}\,. \tag{A.11}$$

The center term

$$\mathcal{B}_{pqr} = \frac{\partial J_{pq}}{\partial \xi_r} \tag{A.12}$$

can be calculated from $X_i = N^a X_i^a$, as

$$J_{pq} = \frac{\partial X_q}{\partial \xi_p} = B_p^{\xi a} X_q^a \,, \tag{A.13}$$

$$\Rightarrow \qquad \mathcal{B}_{pqr} = \frac{\partial J_{pq}}{\partial \xi_r} = H_{pr}^{\xi a} X_q^a \,. \tag{A.14}$$

Finally, the second derivative of the shape function is given by

$$H_{jk} = \frac{\partial^2 N}{\partial X_j \partial X_k} = J_{jm}^{-1} J_{kr}^{-1} H_{mr}^{\xi} - J_{jp}^{-1} \mathcal{B}_{pqr} J_{qm}^{-1} J_{kr}^{-1} B_m^{\xi} \tag{A.15}$$

$$= J_{jm}^{-1} J_{kr}^{-1} (H_{mr}^{\xi} - \mathcal{B}_{mqr} J_{qp}^{-1} B_p^{\xi}) \,. \tag{A.16}$$

Appendix A.4. Third derivative of the shape function

$$K_{jkl} = \frac{\partial^3 N}{\partial X_j \partial X_k \partial X_l} = \frac{\partial}{\partial X_l} \left[J_{jm}^{-1} J_{kr}^{-1} (H_{mr}^{\xi} - \mathcal{B}_{mqr} J_{qp}^{-1} B_p^{\xi}) \right] \tag{A.17}$$

$$= J_{ls}^{-1} \frac{\partial}{\partial \xi_s} \left[J_{jm}^{-1} J_{kr}^{-1} (H_{mr}^{\xi} - \mathcal{B}_{mqr} J_{qp}^{-1} B_p^{\xi}) \right] \tag{A.18}$$

$$= J_{ls}^{-1} (\mathcal{A}_{jms} J_{kr}^{-1} + \mathcal{A}_{krs} J_{jm}^{-1}) (H_{mr}^{\xi} - \mathcal{B}_{mqr} J_{qp}^{-1} B_p^{\xi}) + \tag{A.19}$$

$$J_{ls}^{-1} J_{jm}^{-1} J_{kr}^{-1} (K_{mrs} - C_{mqrs} J_{qp}^{-1} B_p^{\xi} - \mathcal{B}_{mqr} \mathcal{A}_{qps} B_p^{\xi} - \mathcal{B}_{mqr} J_{qp}^{-1} H_{ps}^{\xi}) \,, \tag{A.20}$$

with

$$C_{mqrs} = \frac{\partial \mathcal{B}_{mqr}}{\partial \xi_s} = K_{mrs}^{\xi a} X_q^a \,. \tag{A.21}$$

Appendix B. Consistent stiffness matrix

In this section we provide an approximation of the consistent stiffness matrix used when solving the system of equations (83). This stiffness matrix consists of the contributions of the surface terms $\boldsymbol{K}^e$ and of the volume terms $\boldsymbol{K}^s$

$$\boldsymbol{K} = \sum_e \boldsymbol{K}^e + \sum_s \boldsymbol{K}^s \,. \tag{B.1}$$

It is clear that the forces acting on the interface elements depend on the stress tensors (and on the material tangent moduli) of the two adjacent elements. This increases the implementation complexity and possibly the bandwidth of the assembled global system of equations.

The contributions of the volume integrals $a_{\mathrm{PF}}^e \left(\bar{\boldsymbol{u}}^{\boldsymbol{h}}, \delta \bar{\boldsymbol{u}} \right)$ and $a_{\mathrm{QG}}^e \left(\bar{\boldsymbol{u}}^{\boldsymbol{h}}, \delta \bar{\boldsymbol{u}} \right)$ to the stiffness matrix comprise the conventional first-order term acting on the deformation gradient and the second–order term acting on the gradient of the deformation gradient. The elementary force from the volume integrals reads

$$f_i^{ea} = \int_{\Omega_0^e} \left(\bar{P}_{ij} B_j^a + \bar{Q}_{ijk} H_{jk}^a \right) dB \,, \tag{B.2}$$

From this last equation, the contribution to the global stiffness matrix from each volume element follows as

$$K_{ik}^{eab} = \int_{\Omega_0^e} \left(C_{ijkl} B_j^a B_l^b + \mathcal{L}_{ijklm}^{\bar{F}\bar{G}} B_j^a H_{lm}^b + \mathcal{L}_{ipqkl}^{\bar{G}\bar{F}} H_{pq}^a B_l^b + \mathcal{J}_{ipqklm} H_{pq}^a H_{lm}^b \right) dB \,. \tag{B.3}$$

The contributions of the surface integrals $a^{\mathrm{I1}}_{\mathrm{Ps}}\left(\bar{\boldsymbol{u}}^{\boldsymbol{h}}, \delta\bar{\boldsymbol{u}}\right)$, $a^{\mathrm{I2}}_{\mathrm{Ps}}\left(\bar{\boldsymbol{u}}^{\boldsymbol{h}}, \delta\bar{\boldsymbol{u}}\right)$, $a^{\mathrm{I3}}_{\mathrm{Ps}}\left(\bar{\boldsymbol{u}}^{\boldsymbol{h}}, \delta\bar{\boldsymbol{u}}\right)$, $a^{\mathrm{I1}}_{\mathrm{Qs}}\left(\bar{\boldsymbol{u}}^{\boldsymbol{h}}, \delta\bar{\boldsymbol{u}}\right)$, $a^{\mathrm{I2}}_{\mathrm{Qs}}\left(\bar{\boldsymbol{u}}^{\boldsymbol{h}}, \delta\bar{\boldsymbol{u}}\right)$ and $a^{\mathrm{I3}}_{\mathrm{Qs}}\left(\bar{\boldsymbol{u}}^{\boldsymbol{h}}, \delta\bar{\boldsymbol{u}}\right)$ to the global stiffness matrix are implemented via the interface elements. The surface forces are computed from these surface integrals as

$$
\begin{aligned}
f_k^{sa\pm} = \quad & \pm \int_s N^{a\pm} \left\langle \hat{P}_{kj} \right\rangle \bar{N}_j^- \, d\partial B \\
& + \int_s \left[\!\left[\bar{u}_i^h \right]\!\right] \frac{1}{2} \left(C^{0\pm}_{ijkl} B_l^{a\pm} + \mathcal{L}^{\bar{F}\bar{G}0\pm}_{ijklm} H^{a\pm}_{lm} - \mathcal{L}^{\bar{G}\bar{F}0\pm}_{ijlkm} H^{a\pm}_{ml} - \mathcal{J}^{0\pm}_{ijpkqr} K^{a\pm}_{qrp} \right) \bar{N}_j^- \, d\partial B \\
& \pm \int_s \left[\!\left[\bar{u}_i^h \right]\!\right] \bar{N}_j^- \left\langle \frac{\beta^P}{h^s} C^0_{ijkl} \right\rangle N^{a\pm} \bar{N}_l^- \, d\partial B \\
& \pm \int_s B_j^{a\pm} \left\langle \bar{Q}_{kjl} \right\rangle \bar{N}_l^- \, d\partial B \\
& + \int_s \left[\!\left[\frac{\partial \bar{u}_i^h}{\partial \bar{X}_j} \right]\!\right] \frac{1}{2} \left(\mathcal{J}^{0\pm}_{ijrkpq} H^{a\pm}_{pq} + \mathcal{L}^{\bar{G}\bar{F}0\pm}_{ijrkp} B_p^{a\pm} \right) \bar{N}_r^- \, d\partial B \\
& \pm \int_s \left[\!\left[\frac{\partial \bar{u}_i^h}{\partial \bar{X}_j} \right]\!\right] \bar{N}_l^- \left\langle \frac{\beta^Q}{h^s} \mathcal{J}^0_{ijlkpq} \right\rangle B_p^{a\pm} \bar{N}_q^- \, d\partial B \,,
\end{aligned}
\tag{B.4}
$$

where "±" gives a "+" contribution to the degrees of freedom of the "+" element and a "−" contribution to the degrees of freedom of the "−" element. From this expression, the elementary stiffness matrix is given by

$$
\begin{aligned}
K_{ki}^{sa\pm b\pm} = \quad & \pm + \int_s N^{a\pm} \frac{1}{2} \left(C^{\pm}_{kjil} B_l^{b\pm} + (\mathcal{L}^{\bar{F}\bar{G}\pm}_{kjilm} - \mathcal{L}^{\bar{G}\bar{F}\pm}_{kjlim}) H^{b\pm}_{lm} - \mathcal{J}^{\pm}_{kjpiqr} K^{b\pm}_{qrp} \right) \bar{N}_j^- \, d\partial B \\
& + \pm \int_s N^{b\pm} \frac{1}{2} \left(C^{0\pm}_{ijkl} B_l^{a\pm} + (\mathcal{L}^{\bar{F}\bar{G}0\pm}_{ijklm} - \mathcal{L}^{\bar{G}\bar{F}0\pm}_{ijlkm}) H^{a\pm}_{lm} - \mathcal{J}^{0\pm}_{ijpkqr} K^{a\pm}_{qrp} \right) \bar{N}_j^- \, d\partial B \\
& \pm \pm \int_s N^{b\pm} \bar{N}_j^- \left\langle \frac{\beta^P}{h^s} C^0_{ijkl} \right\rangle N^{a\pm} \bar{N}_l^- \, d\partial B \\
& \pm + \int_s B_j^{a\pm} \frac{1}{2} \left(\mathcal{J}^{\pm}_{kjlipq} H^{b\pm}_{pq} + \mathcal{L}^{\bar{G}\bar{F}\pm}_{kjlip} B_p^{b\pm} \right) \bar{N}_l^- \, d\partial B \\
& + \pm \int_s B_j^{b\pm} \frac{1}{2} \left(\mathcal{J}^{0\pm}_{ijrkpq} H^{a\pm}_{pq} + \mathcal{L}^{\bar{G}\bar{F}0\pm}_{ijrkp} B_p^{a\pm} \right) \bar{N}_r^- \, d\partial B \\
& \pm \pm \int_s B_j^{b\pm} \bar{N}_l^- \left\langle \frac{\beta^Q}{h^s} \mathcal{J}^0_{ijlkpq} \right\rangle B_p^{a\pm} \bar{N}_q^- \, d\partial B \,,
\end{aligned}
\tag{B.5}
$$

where the notation "±±" means the consecutive application of "±" and "±".

References

[1] J. Michel, H. Moulinec, P. Suquet, Effective properties of composite materials with periodic microstructure: a computational approach, Computer Methods in Applied Mechanics and Engineering 172 (1-4) (1999) 109 – 143. doi:10.1016/S0045-7825(98)00227-8.
URL http://www.sciencedirect.com/science/article/pii/S0045782598002278

[2] K. Terada, M. Hori, T. Kyoya, N. Kikuchi, Simulation of the multi-scale convergence in computational homogenization approaches, International Journal of Solids and Structures 37 (16) (2000) 2285–2311. doi:DOI: 10.1016/S0020-7683(98)00341-2.
URL http://www.sciencedirect.com/science/article/B6VJS-3YDFYCH-4/2/788d085d620c6c5ae804d8c4e4f8ae9b

[3] C. Miehe, Strain-driven homogenization of inelastic microstructures and composites based on an incremental variational formulation, Int. J. Numer. Meth. Engng. 55 (11) (2002) 1285–1322.
URL http://dx.doi.org/10.1002/nme.515

[4] C. Miehe, A. Koch, Computational micro-to-macro transitions of discretized microstructures undergoing small strains, Archive of Applied Mechanics 72 (4) (2002) 300–317, 10.1007/s00419-002-0212-2.
URL http://dx.doi.org/10.1007/s00419-002-0212-2

[5] V. Kouznetsova, W. A. M. Brekelmans, F. P. T. Baaijens, An approach to micro-macro modeling of heterogeneous materials, Computational Mechanics 27 (1) (2001) 37–48.
URL http://dx.doi.org/10.1007/s004660000212

[6] V. Kouznetsova, M. G. D. Geers, W. A. M. Brekelmans, Multi-scale constitutive modelling of heterogeneous materials with a gradient-enhanced computational homogenization scheme, Int. J. Numer. Meth. Engng. 54 (8) (2002) 1235–1260.
URL http://dx.doi.org/10.1002/nme.541

[7] V. G. Kouznetsova, M. G. D. Geers, W. A. M. Brekelmans, Multi-scale second-order computational homogenization of multi-phase materials: a nested finite element solution strategy, Computer Methods in Applied Mechanics and Engineering 193 (48-51) (2004) 5525–5550, advances in Computational Plasticity. doi:DOI: 10.1016/j.cma.2003.12.073.
URL http://www.sciencedirect.com/science/article/B6V29-4D4D4JV-3/2/6fd8ac06299b9a26d8a17438871de868

[8] L. Kaczmarczyk, C. J. Pearce, N. Bicanic, Scale transition and enforcement of rve boundary conditions in second-order computational homogenization, Int. J. Numer. Meth. Engng. 74 (3) (2008) 506–522.
URL http://dx.doi.org/10.1002/nme.2188

[9] D. Peric, E. A. de Souza Neto, R. A. Feijóo, M. Partovi, A. J. C. Molina, On micro-to-macro transitions for multi-scale analysis of non-linear heterogeneous materials: unified variational basis and finite element implementation, Int. J. Numer. Meth. Engng.
URL http://dx.doi.org/10.1002/nme.3014

[10] M. G. D. Geers, V. G. Kouznetsova, W. A. M. Brekelmans, Multi-scale computational homogenization: Trends and challenges, Journal of Computational and Applied Mathematics 234 (7) (2010) 2175–2182, fourth International Conference on Advanced COmputational Methods in ENgineering (ACOMEN 2008). doi:DOI: 10.1016/j.cam.2009.08.077.
URL http://www.sciencedirect.com/science/article/B6TYH-4X1J73B-8/2/ee8d9b69133503eaf14b00ddbe1bd8f5

[11] V. G. Kouznetsova, Computational homogenization for the multi-scale analysis of multi-phase materials, Ph.D. thesis, Technische Universiteit Eindhoven (2002).

[12] A. McBride, J. Mergheim, A. Javili, P. Steinmann, S. Bargmann, Micro-to-macro transitions for heterogeneous material layers accounting for in-plane stretch, Journal of the Mechanics and Physics of Solids 60 (6) (2012) 1221 – 1239. doi:10.1016/j.jmps.2012.01.003.
URL http://www.sciencedirect.com/science/article/pii/S0022509612000117

[13] S. Forest, F. Barbe, G. Cailletaud, Cosserat modelling of size effects in the mechanical behaviour of polycrystals and multi-phase materials, International Journal of Solids and Structures 37 (4647) (2000) 7105 – 7126. doi:10.1016/S0020-7683(99)00330-3.
URL http://www.sciencedirect.com/science/article/pii/S0020768399003303

[14] R. A. Toupin, Elastic materials with couple stresses, Archive for Rational Mechanics Analysis 11 (1962) 385–414.

[15] R. D. Mindlin, Micro-structure in linear elasticity, Archive for Rational Mechanics Analysis 16 (1964) 51–78.

[16] R. Mindlin, Second gradient of strain and surface-tension in linear elasticity, International Journal of Solids and Structures 1 (1965) 417–438. doi:No doi.
URL http://isn-csm.mit.edu/literature/1965-IJSS-Mindlin.pdf

[17] N. Fleck, J. Hutchinson, Strain gradient plasticity, Vol. 33 of Advances in Applied Mechanics, Elsevier, 1997, pp. 295 – 361. doi:10.1016/S0065-2156(08)70388-0.
URL http://www.sciencedirect.com/science/article/pii/S0065215608703880

[18] R. Peerlings, R. de Borst, W. Brekelmans, S. Ayyapureddi, Gradient-enhanced damage for quasi-brittle materials, Int. J. Numer. Meth. Engng 39 (1996) 3391–3403.

[19] C. Hirschberger, E. Kuhl, P. Steinmann, On deformational and configurational mechanics of micromorphic hyperelasticity - theory and computation, Comput. Methods. Appl. Mech. Engrg. 196 (2007) 4027–4044.

[20] S.-A. Papanicolopulos, A. Zervos, A method for creating a class of triangular c1 finite elements, International Journal for Numerical Methods in Engineering 89 (11) (2012) 1437–1450. doi:10.1002/nme.3296.
URL http://dx.doi.org/10.1002/nme.3296

[21] S.-A. Papanicolopulos, A. Zervos, I. Vardoulakis, A three-dimensional c1 finite element for gradient elasticity, International Journal for Numerical Methods in Engineering 77 (10) (2009) 1396–1415. doi:10.1002/nme.2449.
URL http://dx.doi.org/10.1002/nme.2449

[22] E. Amanatidou, N. Aravas, Mixed finite element formulations of strain-gradient elasticity problems, Computer Methods in Applied Mechanics and Engineering 191 (1516) (2002) 1723 – 1751. doi:10.1016/S0045-7825(01)00353-X.
URL http://www.sciencedirect.com/science/article/pii/S004578250100353X

[23] J. Y. Shu, W. E. King, N. A. Fleck, Finite elements for materials with strain gradient effects, International journal for numerical methods in engineering 44 (3) (1999) 373–391, eng.
URL http://www.refdoc.fr/Detailnotice?idarticle=11668682

[24] G. Engel, K. Garikipati, T. Hughes, M. Larson, L. Mazzei, R. Taylor, Continuous/discontinuous finite element approximations of fourth-order elliptic problems in structural and continuum mechanics with applications to thin beams and plates, and strain gradient elasticity, Computer Methods in Applied Mechanics and Engineering 191 (34) (2002) 3669 – 3750. doi:10.1016/S0045-7825(02)00286-4.
URL http://www.sciencedirect.com/science/article/pii/S0045782502002864

[25] R. Bala Chandran, Development of discontinuous galerkin method for nonlocal linear elasticity, Master's thesis, Massachusetts Institute of Technology (2007).
URL http://dspace.mit.edu/handle/1721.1/41730

[26] L. Noels, R. Radovitzky, A general discontinuous galerkin method for finite hyperelasticity. formulation and numerical applications, International Journal for Numerical Methods in Engineering 68 (1) (2006) 64–97. doi:10.1002/nme.1699.
URL http://dx.doi.org/10.1002/nme.1699

[27] A. Ten Eyck, A. Lew, Discontinuous galerkin methods for non-linear elasticity, International Journal for Numerical Methods in Engineering 67 (9) (2006) 1204–1243. doi:10.1002/nme.1667.
URL http://dx.doi.org/10.1002/nme.1667

[28] P. Hansbo, M. Larson, A discontinuous galerkin methodfor the plate equation, Calcolo 39 (2002) 41–59, 10.1007/s100920200001.
URL http://dx.doi.org/10.1007/s100920200001

[29] L. Noels, R. Radovitzky, A new discontinuous galerkin method for kirchhofflove shells, Computer Methods in Applied Mechanics and

Engineering 197 (3340) (2008) 2901 – 2929. doi:10.1016/j.cma.2008.01.018.
URL http://www.sciencedirect.com/science/article/pii/S0045782508000376

[30] G. N. Wells, K. Garikipati, L. Molari, A discontinuous galerkin formulation for a strain gradient-dependent damage model, Computer Methods in Applied Mechanics and Engineering 193 (3335) (2004) 3633 – 3645. doi:10.1016/j.cma.2004.01.020.
URL http://www.sciencedirect.com/science/article/pii/S0045782504000921

[31] J. Djoko, F. Ebobisse, A. McBride, B. Reddy, A discontinuous galerkin formulation for classical and gradient plasticity part 1: Formulation and analysis, Computer Methods in Applied Mechanics and Engineering 196 (3740) (2007) 3881 – 3897, special Issue Honoring the 80th Birthday of Professor Ivo Babuska. doi:10.1016/j.cma.2006.10.045.
URL http://www.sciencedirect.com/science/article/pii/S0045782507001144

[32] A. McBride, B. Reddy, A discontinuous galerkin formulation of a model of gradient plasticity at finite strains, Computer Methods in Applied Mechanics and Engineering 198 (2126) (2009) 1805 – 1820, ¡ce:title¿Advances in Simulation-Based Engineering Sciences Honoring J. Tinsley Oden¡/ce:title¿. doi:10.1016/j.cma.2008.12.034.
URL http://www.sciencedirect.com/science/article/pii/S0045782509000152

[33] A. Abdulle, Multiscale method based on discontinuous galerkin methods for homogenization problems, Comptes Rendus Mathematique 346 (12) (2008) 97 – 102. doi:10.1016/j.crma.2007.11.029.
URL http://www.sciencedirect.com/science/article/pii/S1631073X07005158

[34] A. Abdulle, Discontinuous galerkin finite element heterogeneous multiscale method for elliptic problems with multiple scales, Math. Comp. 81 (2012) 687–713.
URL http://dx.doi.org/10.1090/S0025-5718-2011-02527-5

[35] G. Becker, C. Geuzaine, L. Noels, A one field full discontinuous galerkin method for kirchhofflove shells applied to fracture mechanics, Computer Methods in Applied Mechanics and Engineering 200 (4546) (2011) 3223 – 3241. doi:10.1016/j.cma.2011.07.008.
URL http://www.sciencedirect.com/science/article/pii/S0045782511002490

[36] L. Wu, D. Tjahjanto, G. Becker, A. Makradi, A. Jérusalem, L. Noels, A micro-meso-model of intra-laminar fracture in fiber-reinforced composites based on a discontinuous galerkin/cohesive zone method, Engineering Fracture Mechanics.

[37] V.-D. Nguyen, E. Béchet, C. Geuzaine, L. Noels, Imposing periodic boundary condition on arbitrary meshes by polynomial interpolation, Computational Materials Science 55 (0) (2012) 390 – 406. doi:10.1016/j.commatsci.2011.10.017.
URL http://www.sciencedirect.com/science/article/pii/S0927025611005866

[38] C. Geuzaine, J.-F. Remacle, Gmsh: A 3-d finite element mesh generator with built-in pre- and post-processing facilities, International Journal for Numerical Methods in Engineering 79 (11) (2009) 1309–1331.
URL http://dx.doi.org/10.1002/nme.2579

[39] Mark, Ainsworth, Essential boundary conditions and multi-point constraints in finite element analysis, Computer Methods in Applied Mechanics and Engineering 190 (48) (2001) 6323 – 6339. doi:10.1016/S0045-7825(01)00236-5.
URL http://www.sciencedirect.com/science/article/pii/S0045782501002365

[40] A. Zervos, Finite elements for elasticity with microstructure and gradient elasticity, International Journal for Numerical Methods in Engineering 73 (4) (2008) 564–595. doi:10.1002/nme.2093.
URL http://dx.doi.org/10.1002/nme.2093